Master's Thesis

The effect of the curvature of a grain boundary network in the three-dimensional polycrystal on the response to a cyclic thermal loading: an FEM study

Young-Ju Jeon

Department of Materials Science and Engineering

Graduate School of UNIST

2016

The effect of the curvature of a grain boundary network in the three-dimensional polycrystal on the response to a cyclic thermal loading: an FEM study

Young-Ju Jeon

Department of Materials Science and Engineering

Graduate School of UNIST

The effect of the curvature of a grain boundary network in the three-dimensional polycrystal on the response to a cyclic thermal loading: an FEM study

A thesis/dissertation
submitted to the Graduate School of UNIST
in partial fulfillment of the
requirements for the degree of
Master of Science

Young-Ju Jeon

7. 11. 2016
Approved by

_____

Advisor
Sukbin Lee

The effect of the curvature of a grain boundary network in the three-dimensional polycrystal on the response to a cyclic thermal loading: an FEM study

Young-Ju Jeon

This certifies that the thesis/dissertation of Young-Ju Jeon
is approved.

7. 11. 2016

signature

_____

Advisor: Sukbin Lee

signature

_____

typed name: Thesis Committee Member #1: Kisuk Lee

signature

_____

typed name: Thesis Committee Member #2: Juyoung Kim

signature

Abstract

In this work, the effect of curvature of the grain boundary network in a polycrystalline material under external loading on the mechanical field distribution is examined. First, a three-dimensional digital voxellated polycrystal is generated using the Monte Carlo Potts model in the context of normal grain growth. Then, three-dimensional conformal, smoothed surface mesh elements on the grain boundary network of the such a digital microstructure are created using a set of both in-house codes. From surface mesh, the three-dimensional conformal volume elements are created using a commercial package. Finally, a finite element method (ABAQUS) is used on the resultant mesh elements to simulate the mechanical response inside the polycrystal under cyclic thermal loading. Specifically, we compared mechanical fields distribution inside the polycrystal as the grain boundary curvature changes.

Keywords: Polycrystal; Local Mechanical Fields; Finite element analysis; Grain Boundary

Contents

List of figures

Figure 1. The stresses on the face of a unit cube in a homogeneously stress body

Figure 2. Inhomogeneous stress: The force on the face perpendicular to Ox_3 are not shown.

Figure 3. Definition of Bunge Euler angles

Figure 4. Strain energy density

Figure 5. Images of (a) the original surface mesh (smoothed surface mesh of grain boundaries before quality enhancement) (b) re-meshed mesh using the size and bias option, and (c) re-meshed mesh using the quality index option

Figure 6. Images of triangle minimum angle of (a) the original surface mesh (smoothed surface mesh of grain boundaries before quality enhancement) (b) re-meshed mesh using the size and bias option, and (c) re-meshed mesh using the quality index option

Figure 7. Images of Jacobian of (a) the original surface mesh (smoothed surface mesh of grain boundaries before quality enhancement) (b) re-meshed mesh using the size and bias option, and (c) re-meshed mesh using the quality index option

Figure 8. Images of aspect ratio of (a) the original surface mesh (smoothed surface mesh of grain boundaries before quality enhancement) (b) re-meshed mesh using the size and bias option, and (c) re-meshed mesh using the quality index option

Figure 9. Images of the aspect ratios of 3d mesh elements of (a) original surface mesh (smoothed surface mesh of grain boundaries before quality enhancement), (b) 3d mesh elements generated using standard volumetric mesh technique from the surface mesh, re-meshed using the size and bias option, and (c) 3d mesh elements generated using standard volumetric mesh technique from the surface mesh re-meshed using the quality index option. In (d), the aspect ratios from three techniques are compared.

1. Introduction

In ideal, polycrystals are filled with grains without empty space, and those grains have smoothly or monotonically changing boundary curvatures. Many theories on the morphology and evolution of the polycrystalline structures are based on this premise [1-2]. However, when imaging those boundaries (or boundary traces on two-dimensional sections), they appear as a series of discrete steps due to the nature of the imaging grid, or voxels (i.e., pixels in two-dimensions.). Naturally, the three dimensional microstructural images from the Monte Carlo Potts model simulations show the stair-stepped morphology of the grain boundaries. Even though such a simulation gives fairly well-predicted microstructure parameters like grain size distribution, texture, misorientations, and so on, we cannot obtain the correct or, at least, approximated grain boundary normal information. Since some of the properties of polycrystalline materials such as corrosion, creep, fracture and electron transport behavior are known to be a function of crystallographic orientation of grain boundaries, it is important to realistically approximate and characterize the grain boundary networks in a polycrystals.

Recently, much effort to generate conformal surface/volume mesh elements in digital polycrystalline microstructures obtained from both simulations and experiments has been in progress [3-8]. But, to the best author's knowledge, the long-range or local curvatures of the grain boundaries in those reports [3-8] are either distorted or badly approximated due to the application of the rather simple assumptions or the functionals that maximize the quality of the smoothness of the grain boundaries regardless of the physics of constraints on the grain boundary nature. In light of that, in the present study, we generate a conformal surface mesh of a grain boundary network in a digital polycrystal, which maintains the long-range and local curvature of the grain boundaries, based on imges, only. Then, using such an approximated grain boundary surface mesh, a volumetric mesh elements, appropriate for a Finite Element Method (FEM) simulation, are created. When creating surface mesh of the grain boundaries, too. By doing so, one can compare mechanical responses form the same polycrystals according to grain boundary shape like flat or curved in 3Ds.

The proposed research is conducted as follows. First, we obtain a digital polycrystal from the normal grain growth simulation using Monte Carlo Potts model simulation. Second, the grain boundary network in the polycrystal is segmented using the multi-material marching cubes algorithm. Next, we smooth the segmented junctions of the grains using a constrained line smoothing(CLS) method. Also, we smoothed the grain boundaries inside the polycrystal using a constrained Laplacian smoothing(CLpS) method. After improving the surface mesh quality using a commercial package, a set of conformal volumetric tetrahedron elements are created. Finally, we evaluate the mesh quality in the 3D polycrystal and use the polycrystalline mesh as input for an elastic cyclic thermal loading simulation.

2. Theoretical background

2.1 Elasticity

2.1.1 Stiffness coefficient

A solid body changes its shape when subjected to a stress. If a material returns to its original shape when the stress is removed, the material is said to be demonstrating elastic behavior. It is further observed that for sufficiently small stresses the amount of strain is proportional to the magnitude of the applied stress. This is known as Hooke's law.

For example, suppose a bar of an isotropic solid is loaded in pure tension so that the tensile stress is, σ and the longitudinal strain, ε, equals $\Delta l / l$, where Δl is the increase in length and l is the original length of the bar before deformation. Hooke's Law states that

$$\varepsilon = S\sigma \tag{1}$$

, where S is a constant, called the elastic compliance constant or, shortly, the compliance, for the particular arrangement of stress and strain directions. As an alternative we could write

$$\sigma = C\varepsilon \qquad C = 1/S \tag{2}$$

where C is the elastic stiffness constant, or the stiffness. For isotropic cases, C is also called Young's Modulus.

These statements and definitions need to be generalized for an arbitrary, anisotropic case. First of all, a homogeneous strain ε_{ij} is specified, in general, by a second-rank tensor. It is known that, if a general homogeneous stress σ_{ij} is applied to a crystal (figure 1), the resulting homogeneous strain ε_{ij} is such that each component is linearly related to all the components of the stress as follows.

$$\varepsilon_{11} = S_{1111}\sigma_{11} + S_{1112}\sigma_{12} + S_{1113}\sigma_{13}$$
$$S_{1121}\sigma_{21} + S_{1122}\sigma_{22} + S_{1123}\sigma_{23} \tag{3}$$
$$S_{1131}\sigma_{31} + S_{1132}\sigma_{32} + S_{1133}\sigma_{33}$$

We have eight more similar equations for the other eight components of ε_{ij}, where S is a 4th rank

2

tensor. The generalized form of Hooke's Law may therefore be written as

$$\varepsilon_{ij} = S_{ijkl}\sigma_{kl} \tag{4}$$

The S_{ijkl} are the compliances of the crystal. Equation (4) stands for nine equations, each with nine terms on the right-hand side. There are 81 S_{ijkl} coefficients. As an alternative to equations (4) the stresses may be expressed in terms of the strain by the equations,

$$\sigma_{ij} = C_{ijkl}\varepsilon_{kl} \tag{5}$$

where the C_{ijkl} are the 81 stiffness constants of the crystal. The physical meaning of the stiffness tensor is appreciated by imagining the crystal to be subjected to various simple stress conditions.

Suppose a shear stress were applied, and both σ_{12} and σ_{21} would be present and we should have

$$\varepsilon_{11} = S_{1112}\sigma_{12} + S_{1121}\sigma_{21} = (S_{1112} + S_{1121})\ \sigma_{12} \tag{6}$$

S_{1112} and S_{1121} always occur together; it follows that it is in principle impossible to devise an experiment by which S_{1112} can be separated from S_{1121}. Therefore, to avoid an arbitrary constant we set the two components equal:

$$S_{ijkl} = S_{ijlk} \tag{7}$$

If, on the other hand, a uniaxial tension were applied parallel to Ox_3 the components of strain would be given be

$$\varepsilon_{11} = S_{1133}\sigma_{33}\ ,\ \ \varepsilon_{22} = S_{2233}\sigma_{33}\ \ \text{and so on} \tag{8}$$

But, from the definition of the components of the strain tensor $\varepsilon_{12} = \varepsilon_{21}$. Hence, $S_{1233} = S_{2133}$ and, in general, by considering other special cases, we see that

$$S_{ijkl} = S_{jikl} \tag{9}$$

On account of the relations (7) and (9), only 36 of the 81 components S_{ijkl} are independent.
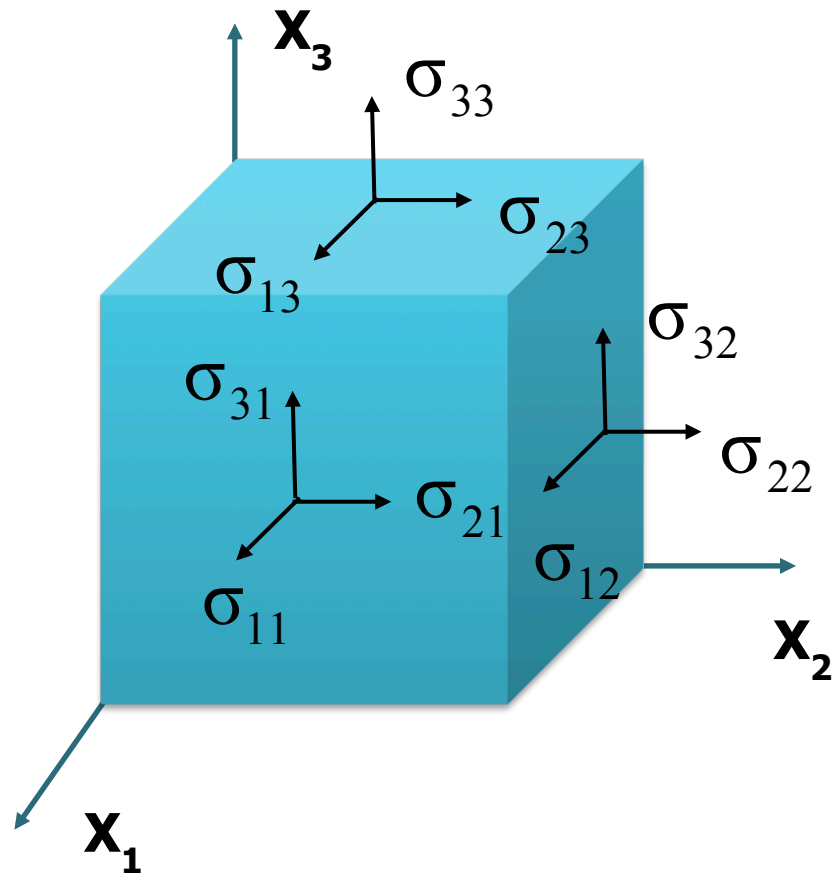
Figure 1. The stresses on the face of a unit cube in a homogenously stress body

In the S_{ijkl} and the C_{ijkl} the first two suffixes are abbreviated into a single one running from 1 to 6, and the last two are abbreviated in the same way. In this way, we convert the tensor notation to the matrix notation.

Tensor notation	11	22	33	23,32	31, 13	12,21
Matrix notation	1	2	3	4	5	6

In matrix format, the stress-strain relation showing the 36 independent components of stiffness can be represented as:

$$
\begin{pmatrix} \sigma_1 \\ \sigma_2 \\ \sigma_3 \\ \sigma_4 \\ \sigma_5 \\ \sigma_6 \end{pmatrix} = \begin{pmatrix} C_{11} & C_{12} & C_{13} & C_{14} & C_{15} & C_{16} \\ C_{21} & C_{22} & C_{23} & C_{24} & C_{25} & C_{26} \\ C_{31} & C_{32} & C_{33} & C_{34} & C_{35} & C_{36} \\ C_{41} & C_{42} & C_{43} & C_{44} & C_{45} & C_{46} \\ C_{51} & C_{52} & C_{53} & C_{54} & C_{55} & C_{56} \\ C_{61} & C_{62} & C_{63} & C_{64} & C_{65} & C_{66} \end{pmatrix} \begin{pmatrix} \varepsilon_1 \\ \varepsilon_2 \\ \varepsilon_3 \\ \varepsilon_4 \\ \varepsilon_5 \\ \varepsilon_6 \end{pmatrix}
$$

Or in short notation, we can write

$$ \sigma_i = C_{ij}\varepsilon_j \quad \text{and} \quad \varepsilon_i = C_{ij}\sigma_j \tag{10} $$

Further reductions in the number of independent constants are possible by employing other symmetry considerations to eq. (10). Of the 36 constants, there are six constants where $i = j$, leaving 30 constants where $i \neq j$. One half of the constants where $i \neq j$ since are independent constants $C_{ij} = C_{ji}$. Therefore, for the general anisotropic linear elastic solid there are 21 independent elastic constant.

As an example, the number of independent elastic constants in cubic system is three as shown below.

$$
\begin{bmatrix}
C_{11} & C_{12} & C_{12} & 0 & 0 & 0 \\
. & C_{11} & C_{12} & 0 & 0 & 0 \\
. & . & C_{11} & 0 & 0 & 0 \\
. & . & . & C_{44} & 0 & 0 \\
. & . & . & . & C_{44} & 0 \\
. & . & . & . & . & C_{44}
\end{bmatrix}
$$

As mentioned before, C_{ijkl} is a fourth-rank tensor. A fourth-rank tensor is defined, like tensors of lower rank, by its transformation law. The 81 numbers C_{ijkl} representing a physical quantity are said to form a fourth rank tensor if they transform on change of axes to C'_{ijkl},

$$
C'_{ijkl} = A_{im}A_{jn}A_{ko}A_{ip}C_{mnop} \tag{11}
$$

where A is rotation matrix.

2.1.2 Constitutive equation

In many real cases, the actual stresses are inhomogeneous, which means the stress components vary from point to point within the body. Consider a rectangular element within the stressed body, where σ_{ij} centered on the origin, and with edges parallel to the axis and of lengths δx_1, δx_2, δx_3 as shown in figure 2. Suppose that stress within the body has a linear gradient in all directions. Then, we find the equation of motion of the element in the face perpendicular to Ox_1 direction as follows. The values of the stress components over the two faces perpendicular to Ox_1 are shown in figure 2. The forces in the Ox_1 direction on these two faces are

$$
-\left(\sigma_{11} - \frac{\partial \sigma_{11}}{\partial x_1}\cdot\frac{1}{2}\delta x_1\right)\delta x_2 \delta x_3 \qquad \text{and} \qquad \left(\sigma_{11} - \frac{\partial \sigma_{11}}{\partial x_1}\cdot\frac{1}{2}\delta x_1\right)\delta x_2 \delta x_3 \tag{12}
$$

so that the resultant sum of the stress is

$$\frac{\partial \sigma_{11}}{\partial x_1}\delta x_1 \delta x_2 \delta x_3$$

Similarly, we find the results for the two faces perpendicular to Ox_2, Ox_3.

$$\frac{\partial \sigma_{12}}{\partial x_2}\delta x_1 \delta x_2 \delta x_3 \quad \text{and} \quad \frac{\partial \sigma_{13}}{\partial x_3}\delta x_1 \delta x_2 \delta x_3$$

If all parts of the body are in static equilibrium, the sum of the three terms above must be equal to zero and, since the volume of the element cannot be zero, we obtain the following equation.

$$\frac{\partial \sigma_{11}}{\partial x_1} + \frac{\partial \sigma_{12}}{\partial x_2} + \frac{\partial \sigma_{13}}{\partial x_3} = 0 \text{, i.e., } \nabla \sigma_{ij} = 0 \tag{13}$$
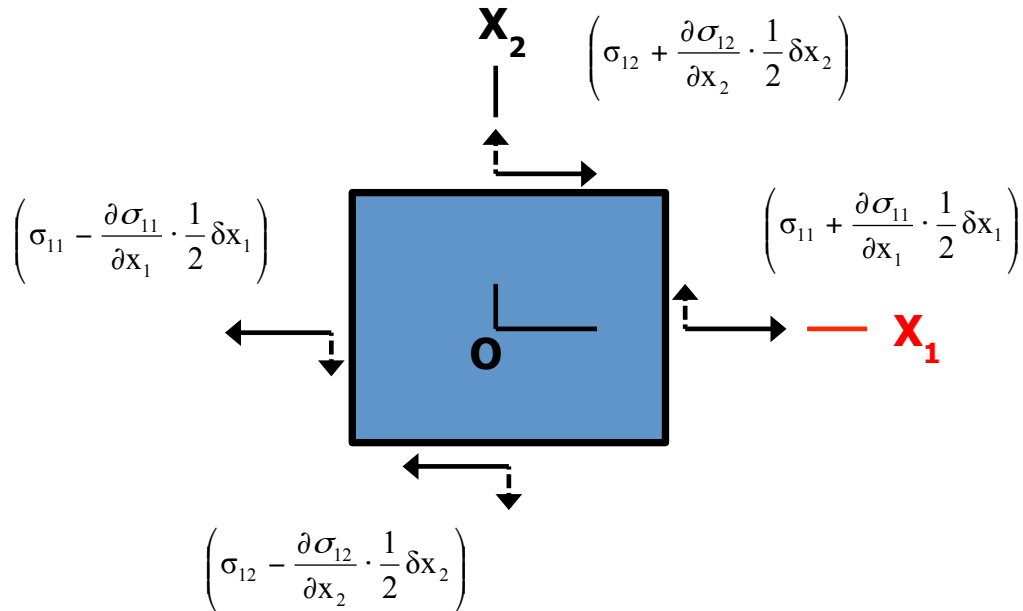
Figure 2. Inhomogeneous stress:
The force on the face perpendicular to Ox_3 are not shown.

7

2.1.3 Thermal expansion coefficient

If the temperature of a crystal changes, crystal tends to shrink or expand, the resulting deformation may be specified by the strain tensor [ε_{ij}]. When a small temperature change ΔT takes place uniformly through out the crystal the deformation is homogenous, and it is found that all the components of [ε_{ij}] are proportional to ΔT;

$$\varepsilon_{ij} = \alpha_{ij}\Delta T \qquad (14)$$

where the α_{ij} is a second rank tensor, the coefficients of thermal expansion.

2.2 Material orientation

2.2.1 Bunge Euler angle

The Euler angles are defined as a set of consecutive rotation angles required for a Cartesian coordinate system to coincide with the other. In representing the orientation of the crystals, they are usually the consecutive angles to rotate the specimen coordinate system to crystal coordinate system. Mathematically, we need three angles for such rotations. The most commonly used are those formulated by Bunge, as shown figure 3. The rotations are:

1. ϕ_1 about the normal direction ND; Z_1

2. Φ about the axis RD'; X (in its new orientation);

3. ϕ_2 about the axis ND' ; Z_2 (in its new orientation)

, where ϕ_1 , Φ , ϕ_2 are the Euler angles (Bunge notation). The effect of the operation sequence of these three rotations can be followed on figure 3.
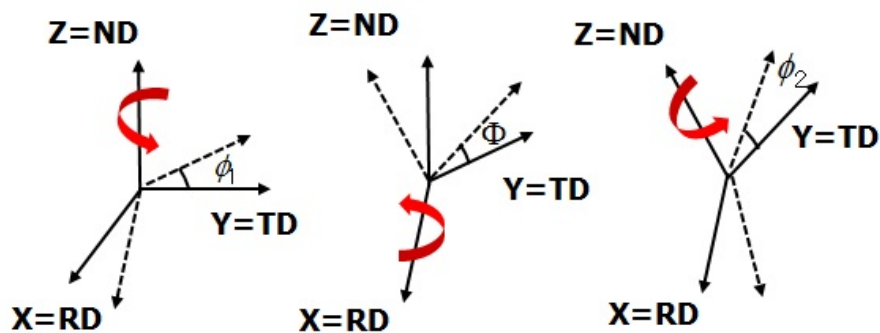
Figure 3. Definition of Bunge Euler angles

Analytically, each three rotations are expressed as a rotation matrix, respectively.

$$R_{\phi_1} = \begin{pmatrix} \cos\phi_1 & \sin\phi_1 & 0 \\ -\sin\phi_1 & \cos\phi_1 & 0 \\ 0 & 0 & 1 \end{pmatrix} \tag{15}$$

$$R_{\Phi} = \begin{pmatrix} 1 & 0 & 0 \\ 0 & \cos\Phi & \sin\Phi \\ 0 & \sin\Phi & \cos\Phi \end{pmatrix} \tag{16}$$

$$R_{\phi_2} = \begin{pmatrix} \cos\phi_2 & \sin\phi_2 & 0 \\ -\sin\phi_2 & \cos\phi_2 & 0 \\ 0 & 0 & 1 \end{pmatrix} \tag{17}$$

By multiplication of these three matrices, an expression of a new rotation matrix, R=[g_{ij}] is obtained which links the result of three consecutive rotations to the Bunge Euler angles :

$$R = R_{\phi_2} \cdot R_{\Phi} \cdot R_{\phi 1} \tag{18}$$

The elements of matrix in terms of the Euler angles are therefore given by

$$
\begin{aligned}
g_{11} &= \cos\phi_1 \cos\phi_2 - \sin\phi_1 \sin\phi_2 \cos\Phi \\
g_{12} &= \sin\phi_1 \cos\phi_2 + \cos\phi_1 \sin\phi_2 \cos\Phi \\
g_{13} &= \sin\phi_2 \sin\Phi \\
g_{21} &= -\cos\phi_1 \sin\phi_2 - \sin\phi_1 \cos\phi_2 \cos\Phi \\
g_{22} &= -\sin\phi_1 \sin\phi_2 + \cos\phi_1 \cos\phi_2 \cos\Phi \\
g_{23} &= \cos\phi_2 \sin\Phi \\
g_{31} &= \sin\phi_1 \sin\Phi \\
g_{32} &= \cos\phi_1 \sin\Phi \\
g_{33} &= \cos\Phi
\end{aligned}
\tag{19}
$$

2.4 von Mises stress and strain energy density

In an elastic, isotropic body subjected to force, a complex three dimensional system of stresses is developed. At any point there are stresses acting in different directions, and the direction and magnitude of stresses changes from point to point. The von Mises stress is expressed as a function of the normal stress and shear stress, giving the yield criteria of the material.

$$\sigma_{vms}^2 = \frac{1}{2}\left[\left(\sigma_{11}-\sigma_{22}\right)^2 + \left(\sigma_{22}-\sigma_{33}\right)^2 + \left(\sigma_{33}-\sigma_{11}\right)^2 + 6\left(\sigma_{23}^2 + \sigma_{31}^2 + \sigma_{12}^2\right)\right] \tag{20}$$

When a stress is applied to material, deformation occurs. The energy stored in a body due to deformation is called the strain energy. The strain energy density of a material is defined as the strain energy per unit volume. In the case of uniaxial stress state, it is equal to the area under the stress-strain curve in figure 4.
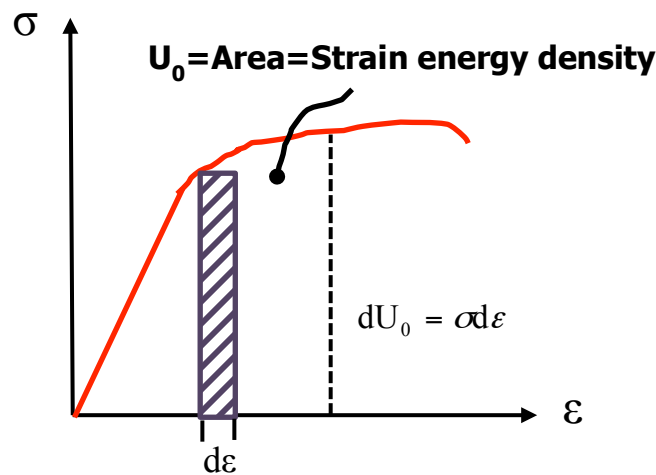
Figure 4. Strain energy density

Strain energy density:

$$U_0 = \int_0^{\varepsilon} \sigma \varepsilon \tag{21}$$

Uniaxial tension test:

$$U_0 = \int_0^{\varepsilon} \sigma \, d\varepsilon = (E\varepsilon) d\varepsilon = \frac{E\varepsilon}{2} = \frac{1}{2}\sigma\varepsilon \tag{22}$$

Strain energy density is a scaler value and defined as, the sum of the multiplication of stress components and strain components as follows.

$$U_0 = \frac{1}{2}\left[\sigma_{11}\varepsilon_{11} + \sigma_{22}\varepsilon_{22} + \sigma_{33}\varepsilon_{33} + \tau_{12}\gamma_{12} + \tau_{23}\gamma_{23} + \tau_{13}\gamma_{13}\right] \tag{23}$$

3. Generation of the mesh elements in 3D polycrystals

3.1 Introduction

In this section, we propose a method for generating a volumetric mesh in a three-dimensional polycrystal using a grain boundary surface mesh. First, a digital polycrystalline microstructure is generated using the Monte Carlo Potts model in the context of normal grain growth. Then, a surface meshing technique is applied on the digital, voxellated microstructure to extract a surface mesh of the grain boundary network, while maintaining characteristics of grain boundaries and grains. To improve the quality of the surface mesh elements, we used a re-meshing technique provided in commercial mesh program (HyperMesh). Once we have an approximated, smoothed mesh of the grain boundary network in the polycrystal, the tetrahedral volumetric mesh elements are created inside each volume, i.e., grains, from the conformal surface mesh. Element quality is measured by using triangle minimum angle, jacobian, aspect ratio and tetra collapse ratio, in order to validate that the volumetric elements are suitable for a finite element analysis as a whole.

3.2 Method

3.2.1 Creating surface mesh of the curved grain boundary network

The first step is to extract the three-dimensional grain boundaries in a cubic gridded digital microstructure and to segment them using the marching cubes algorithm. Next step is to smooth grain junctions and grain boundaries to create a realistic, curvature-maintained grain boundary network. The CLS (constrained line smoothing) algorithm in in-house codes transforms stair-stepped triple junctions into a smooth string of line segments among neighboring grains. While the CLS method is applied, triple junctions move towards the center of local curvature, leading to changes in the volumes of neighboring grains for most of the cases. In the in-house codes, such smoothing is performed with a constriction that the changes in volumes of the neighboring grains are within a prescribed small value. By using a constrained Laplacian smoothing (CLpS) method, grain boundaries inside the polycrystals are also smoothed, while neighboring grains tend to maintain their original volumes.

3.2.2 Re-meshing of the approximated grain boundary network from in-house codes

Curved grain boundary surface mesh from the in-house codes generates small fraction of triangle elements with bad quality, especially in triple junctions regions. Even though they are small in numbers, we need to eliminate those triangles or improve their quality before using them as bounding surfaces for volume meshing. Using a commercial program, we successfully re-meshed the surface mesh. There are a couple of different options for re-meshing such as size and bias, QI

optimize, edge deviation, surface deviation, rigid body mesh. Size and bias option re-meshes existing meshes with constant size. Using QI optimize option, the surface is re-meshed to optimize the quality index (QI) of the elements generated. Edge deviation option sets specific meshing parameters to limit how far the mesh elements can deviate from the actual edges of the surface meshed. Surface deviation option is used to mesh within limits of element deviation from a surface. Rigid body meshing produces a poor quality mesh, but accurately models the surface shapes. In this paper, "size and bias" and "quality index" re-meshing techniques are used.

The quality of elements is visualized and measured using the open-source software called "paraview". The following element quality criteria are known to be satisfied for a Finite element simulation. In shell element, triangle minimum angle > 20, jacobian > 0.6, aspect ratio < 5. Jacobian measures the deviation of an element from its ideal or perfect shape such as a triangle's deviation from equilateral. The jacobian value ranges from 0 to 1, where 1 represents a perfect shaped element. The aspect ratio(AR) is longest edge of an element to its shortest edge. It is suggested that AR be less than 5.

3.2.3 Generation of the volumetric mesh from the surface mesh

Now, we have a curved grain boundary network. A volumetric mesh of the polycrystal can be created based on such a conformal surface mesh dataset. Various options for creating volumetric mesh elements from well-defined surface boundaries like standard, aggressive, gradual, interpolate meshing, and etc. are provided in HyperMesh. In general cases, standard option is used. Aggressive option has smaller number of elements than standard option and the growth rate of the elements is higher inside the volume then the boundary regions of the volume. Gradual option has much more elements than the standard option and the growth rate of the elements is lower inside than the outside. Interpolation option is creating the mesh of which the size is interpolated from the mesh size of the surface region. In this paper, "standard" and "aggressive" meshing techniques are used.

Mesh quality requirement for an FEM simulation using three-dimensional tetrahedron elements is aspect ratio < 5, tetra collapse ratio > 0.5, respectively. Collapse ratio is the ratio between the smallest of h from each node to the longest edge of the tetrahedron, where h is the perpendicular distance from a node to the opposite face.

3.3 Results & Discussion

The approximated, smooth surface mesh of the grain boundaries before quality enhancement (let us call it "original surface mesh") has many artifacts as shown in figure 5 (a). In the figure, (b) and (c) are quality-enhanced surface mesh and have relatively uniform triangles on the surface. In contrast, the original surface mesh, (a), has nonuniform triangles, especially in the regions of grain traces and triple junctions, and, therefore, grain boundary regions are observed by naked eyes. This is why we decided to improve the surface mesh quality before generating volumetric mesh out of it. We perform this procedure using a commercial program called "HyperMesh". In figure 6, the change in the triangle minimum angles after the quality enhancement is shown. Clearly, the minimum angle increases from 20 degree for the original surface mesh to 30 degree after quality enhancement. Moreover, most of the angles have values between 50 to 60 degree, leading to a right-hand skewed distribution of the minimum angles of the triangles in the mesh. Figure 7 shows the Jacobian values of the original surface mesh, (a), and the quality enhanced meshes, (b) and (c), respectively. Most of the triangular elements are enhanced to have the Jacobian values close to 1, and, again, the distributions are skewed to the right after the re-meshing procedures. In figure 8, the change in the aspect ratio is shown and, as expected, the values decrease for the enhanced surface meshes, less than 1.5. Although the original surface mesh satisfies the quality criterion in terms of the aspect ratio, the qualities of the re-meshed surface meshes are better than before, for the distributions become skewed to the ideal value, 1.

By using both the standard and the aggressive techniques, volumetric mesh elements are created. Volumetric meshes from the quality-enhanced surface meshes are found to have better quality than that created from the original surface mesh (before quality-enhancement). In conclusion, it is found that the standard technique produces better volumetric, tetrahedral elements than the aggressive technique. The minimum value of the aspect ratio for the standard case is smaller than that for the aggressive one (figures 9 and 10), while the tetra collapse ratio (figures 11 and 12) increases. The results meet the set of criteria for an FEM simulations.

Based on the results above, one can say that the triangle mesh quality is successfully improved by the re-meshing techniques provided by the commercial program. Using a couple of assorted volumetric mesh generation techniques, like the standard option and the aggressive option, conformal tetrahedral mesh elements on a digital microstructure, appropriate for an Finite Element Method (FEM) simulation, are successfully created, too.

(a)

(b)

(c)

Figure 5. Images of (a) the original surface mesh (smoothed surface mesh of grain boundaries before quality enhancement) (b) re-meshed mesh using the size and bias option, and (c) re-meshed mesh using the quality index option

Figure 6. Images of the triangle minimum angle of (a) the original surface mesh (smoothed surface mesh of grain boundaries before quality enhancement), (b) re-meshed mesh using the size and bias option, and (c) re-meshed mesh using the quality index option

16
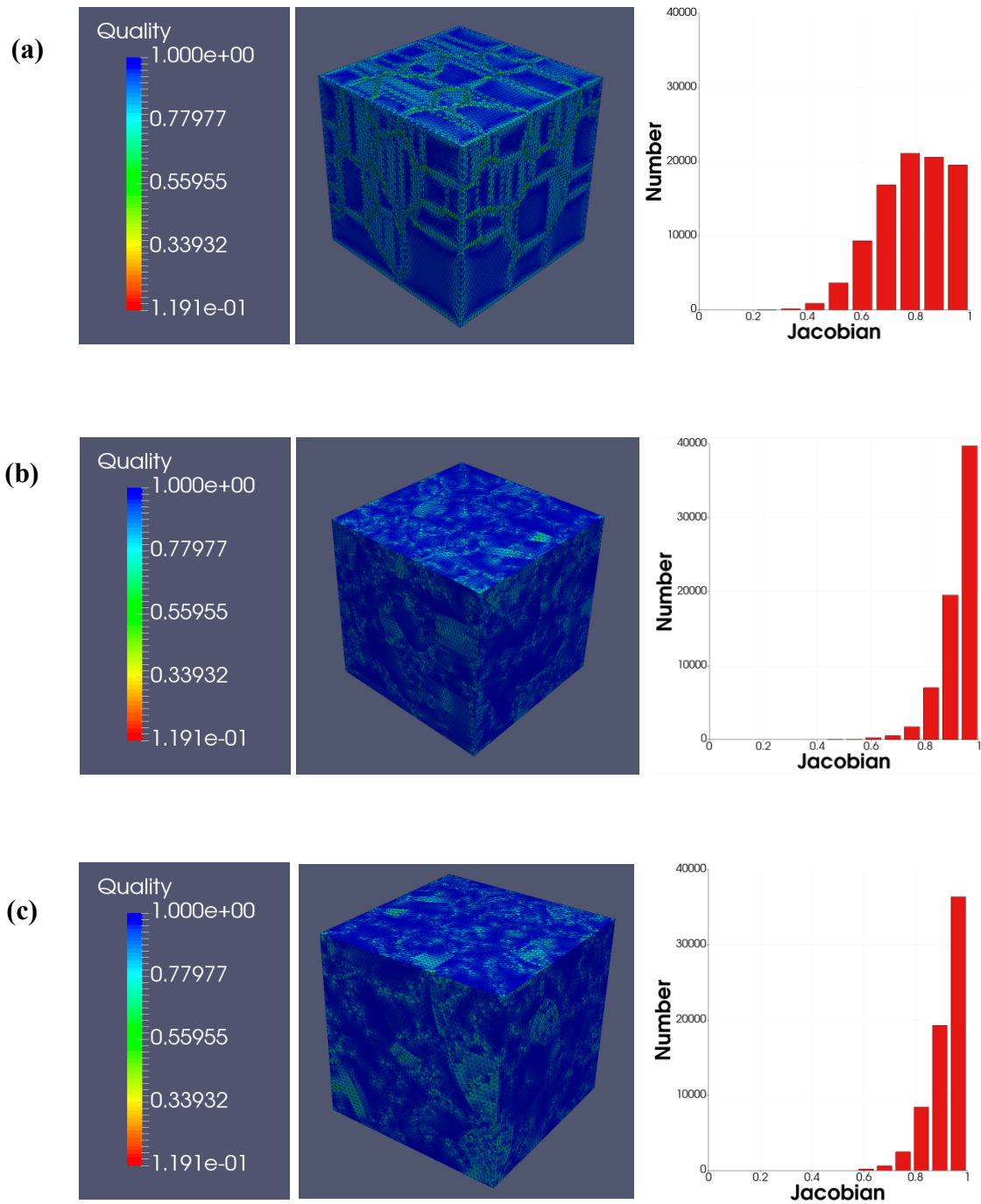
Figure 7. Images of the Jacobian of (a) the original surface mesh (smoothed surface mesh of grain boundaries before quality enhancement), (b) re-meshed mesh using the size and bias option, and (c) re-meshed mesh using the quality index option
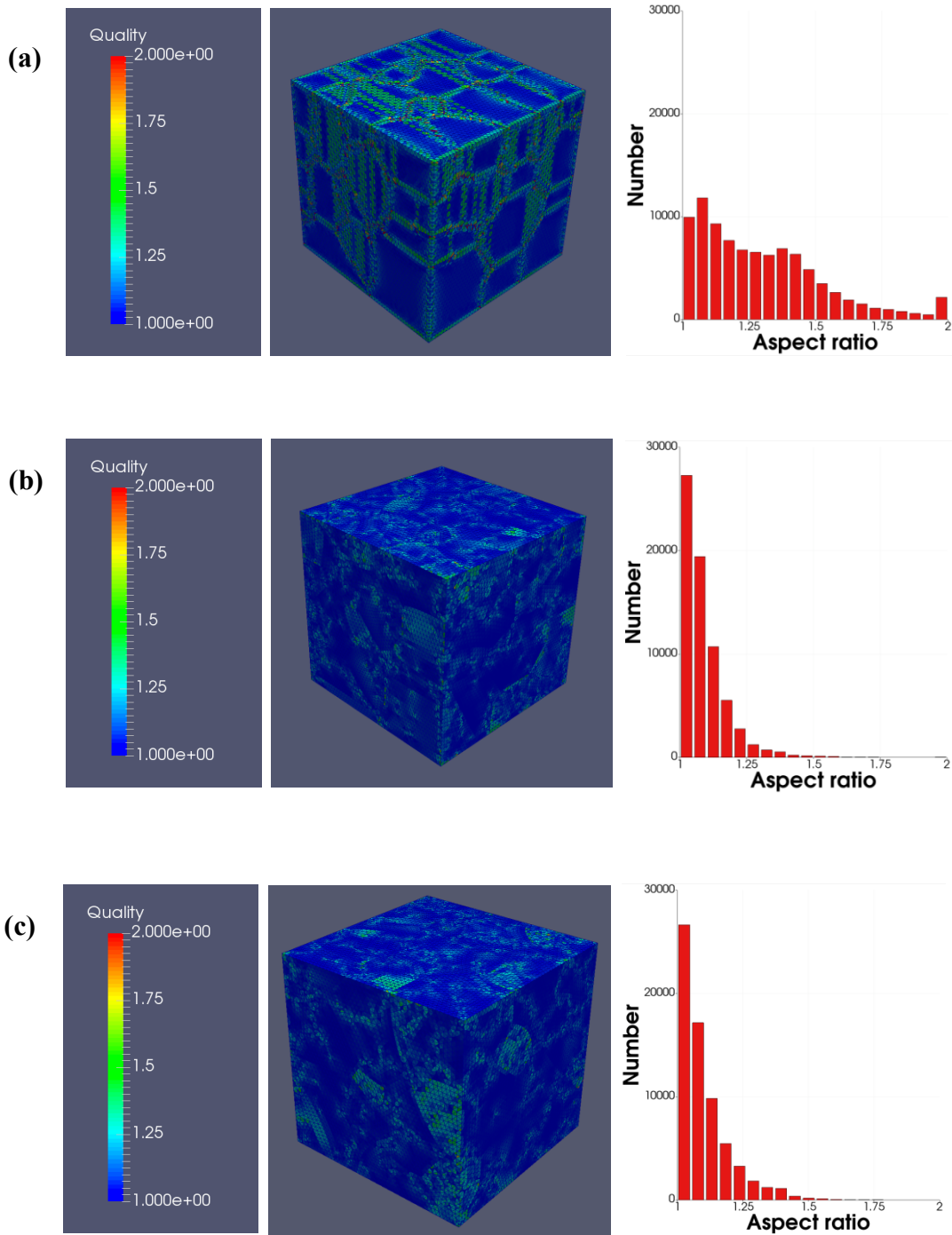
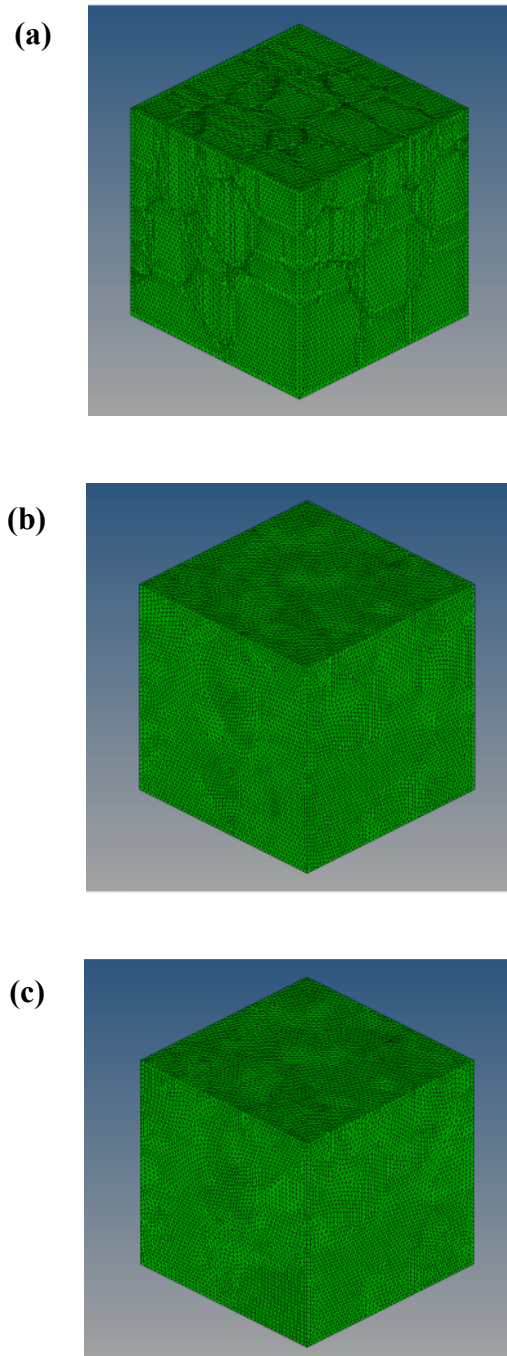Figure 8. Images of the aspect ratio of (a) the original surface mesh (smoothed surface mesh of grain boundaries before quality enhancement), (b) re-meshed mesh using the size and bias option, and (c) re-meshed mesh using the quality index option
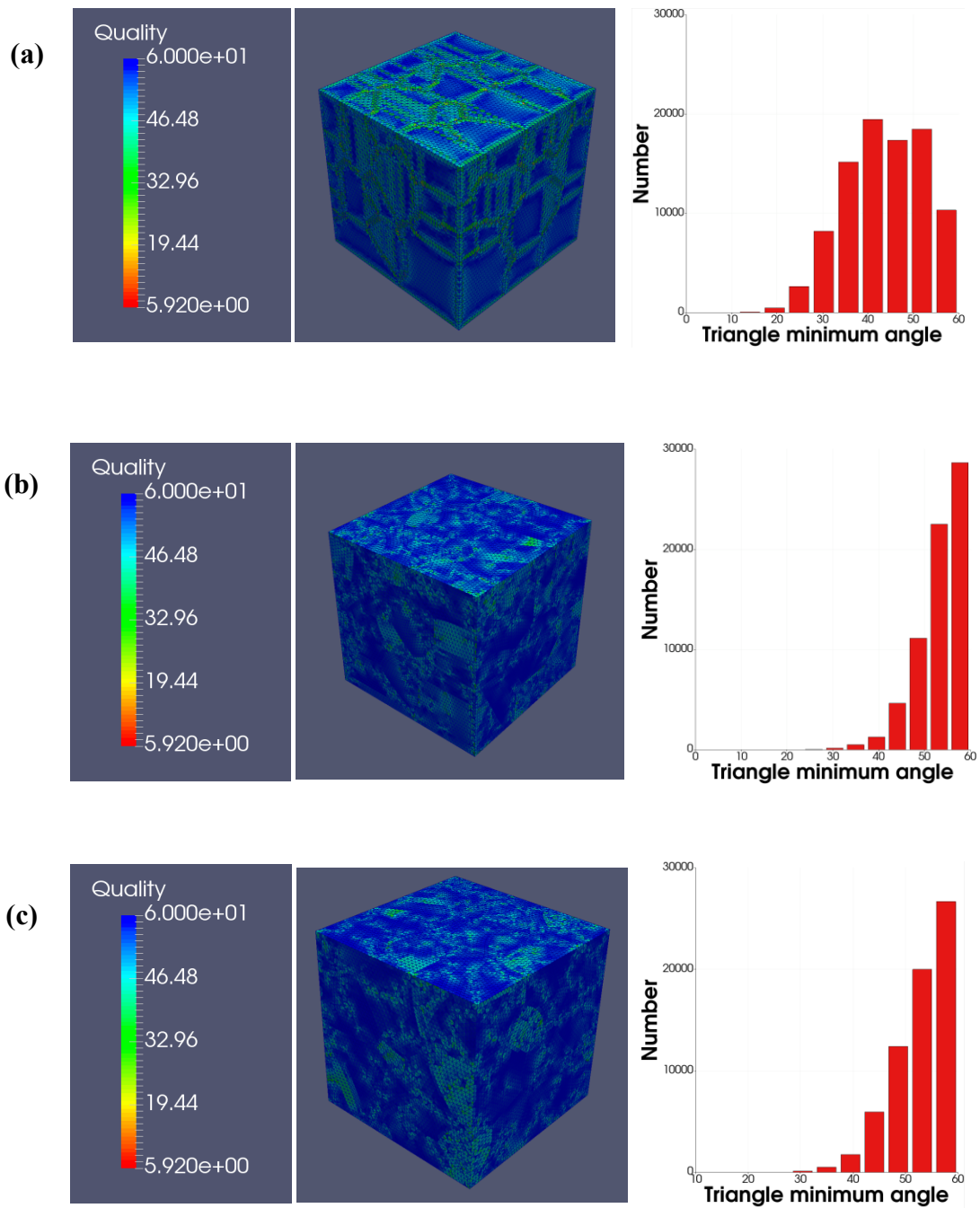
Figure 9. Images of the aspect ratios of 3d mesh elements of (a) original surface mesh (smoothed surface mesh of grain boundaries before quality enhancement), (b) 3d mesh elements generated using standard volumetric mesh technique from the surface mesh, re-meshed using the size and bias option, and (c) 3d mesh elements generated using standard volumetric mesh technique from the surface mesh re-meshed using the quality index option. In (d), the aspect rations from three techniques are compared.

19

Figure 10. Images of the aspect ratios of 3d mesh elements of (a) original surface mesh (smoothed surface mesh of grain boundaries before quality enhancement), (b) 3d mesh elements generated using aggressive volumetric mesh technique from the surface mesh, re-meshed using the size and bias option, and (c) 3d mesh elements generated using aggressive volumetric mesh technique from the surface mesh re-meshed using the quality index option. In (d), the aspect ratios from three techniques are compared.
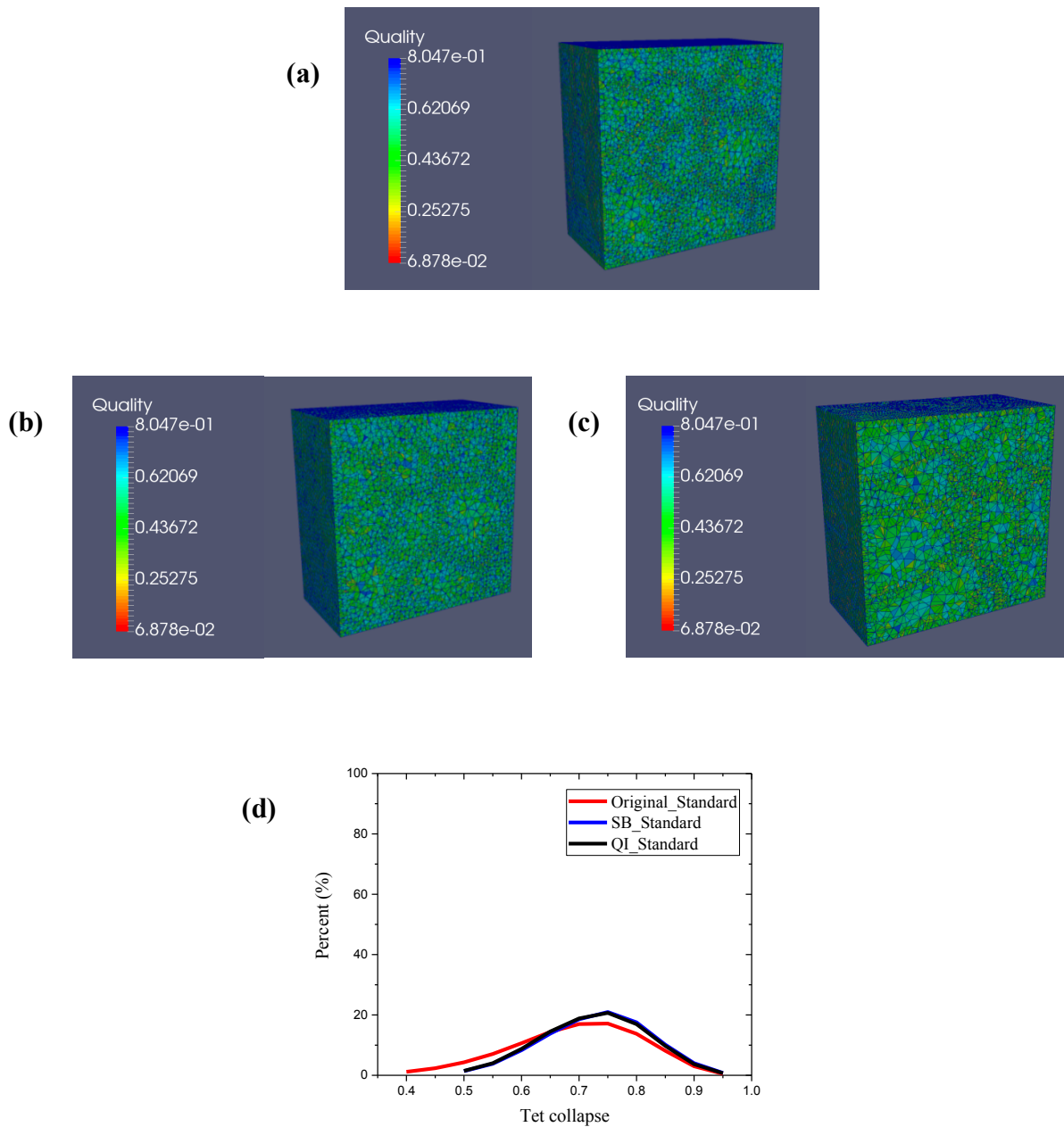
Figure 11. Images of the tetra collapse ratio of 3d mesh elements of (a) original surface mesh (smoothed surface mesh of grain boundaries before quality enhancement), (b) 3d mesh elements generated using standard volumetric mesh technique from the surface mesh, re-meshed using the size and bias option, and (c) 3d mesh elements generated using standard volumetric mesh technique from the surface mesh re-meshed using the quality index option. In (d), the tetra collapse ratios from three techniques are compared.
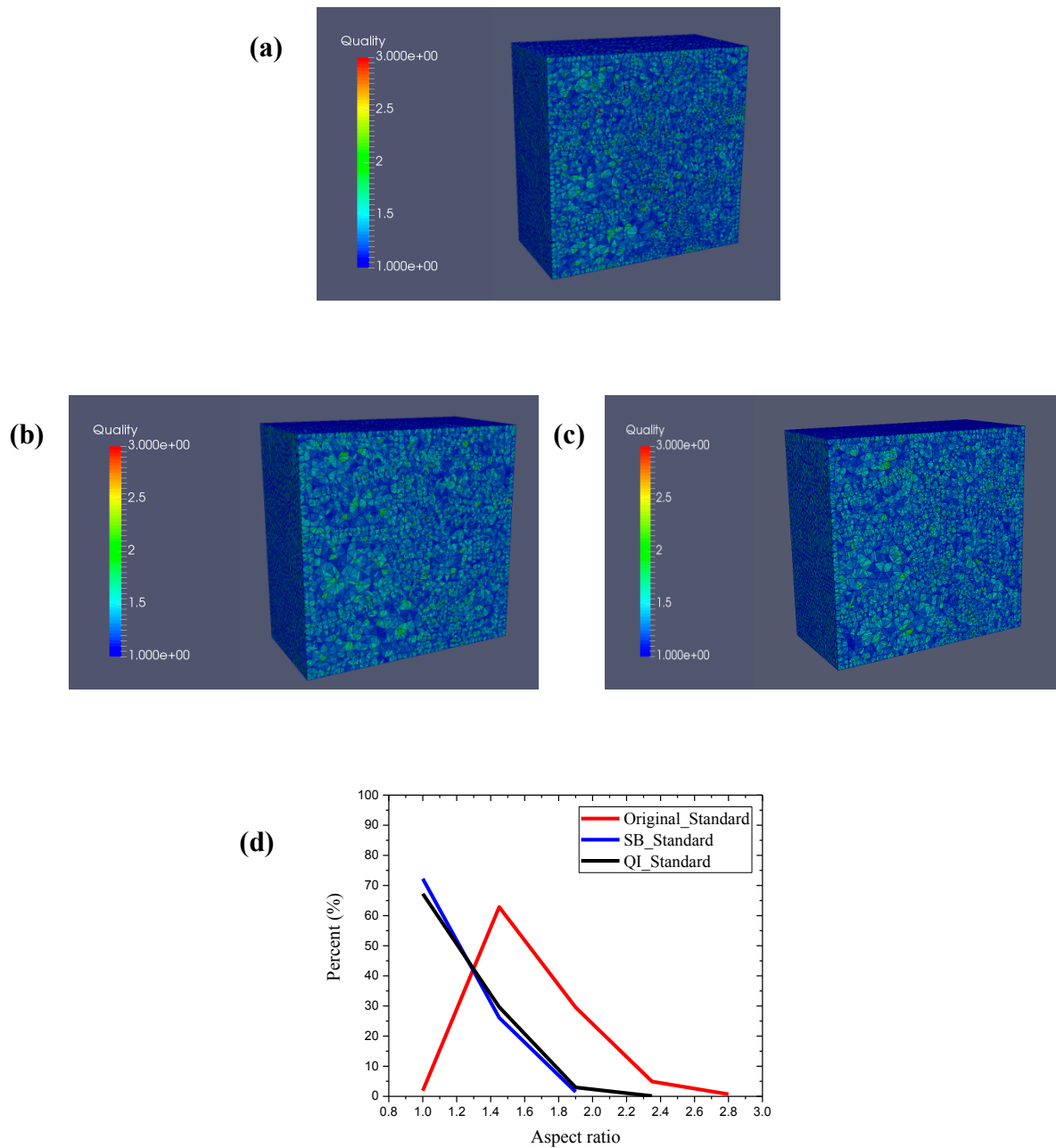
21

Figure 12. Images of the tetra collapse ratio of 3d mesh elements of (a) original surface mesh (smoothed surface mesh of grain boundaries before quality enhancement), (b) 3d mesh elements generated using aggressive volumetric mesh technique from the surface mesh, re-meshed using the size and bias option, and (c) 3d mesh elements generated using aggressive volumetric mesh technique from the surface mesh re-meshed using the quality index option. In (d), the tetra collapse ratios from three techniques are compared.
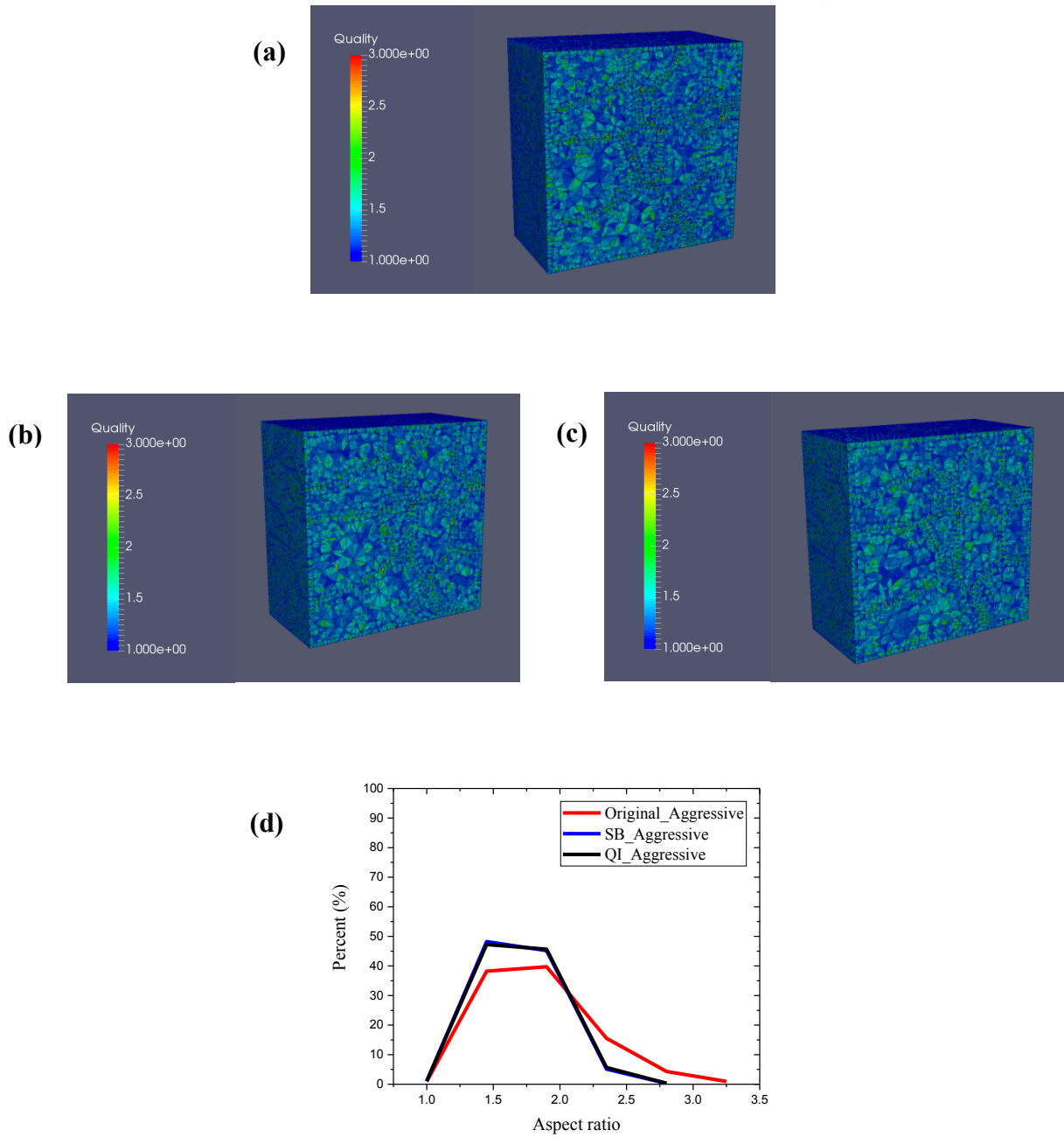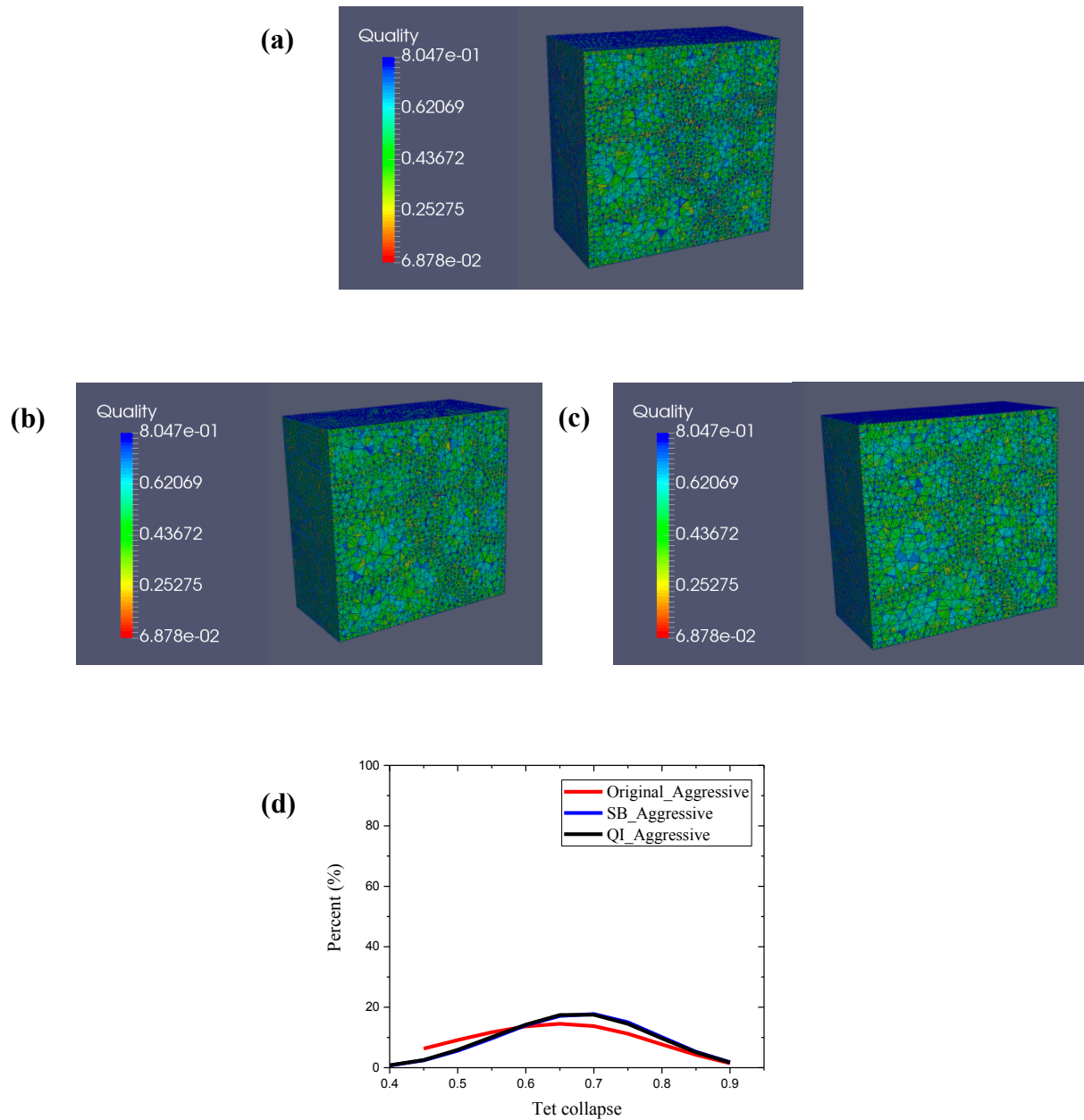
4. Finite Element Modelling using the 3D mesh elements on a polycrystal

4.1 Introduction

When a polycrystalline material is subject to deformation, it has inhomogeneous deformation behavior due to the distribution of the crystallographic orientations of grains, i.e., texture. In a nutshell, stress and strain are localized at the grain boundary and grain junction regions, and have different values and gradient inside grains due to the difference in their crystallographic orientations and surroundings. Therefore, the differences in morphologies and texture of the grains collectively affects the mechanical characteristics of the polycrystal under action, like deformation and fracture behavior. The grain boundaries play important role in the mechanical behavior of polycrystalline material [9-13] as much as the morphology and crystallographic orientation of the grains inside the polycrystal.

However, the polycrystals, obtained through many simulations and meshing procedures, have usually the grain boundaries with distorted long-range and local curvatures. Since the curvature of the grain boundary may affect some of the physical properties of the polycrystalline materials such as corrosion, creep, electronic transport, and so on, it is necessary to generate more realistic 3D polycrystalline mesh elements with grain boundary curvature maintained. Once such 3d elements are created, we can compare the mechanical responses to a set of boundary conditions of both microstructures with flat and curved grain boundaries, for example.

In this section, we take our main focus on the difference in the mechanical fields according to the change in the grain boundary curvature in the polycrystal under a cyclic thermal loading condition. In order to do that, a digital three-dimensional polycrystal is generated using the Monte Carlo algorithm for normal grain growth. In the polycrystal, there are 50 grains and they are assigned with a randomly genereated crystallographic orientation. A commercial Finite Element Modelling package, ABAQUS, is used in order to simulate the mechanical field distribution inside the polycrystal under a cyclic loading condition. The results show that the local stress and strain in the polycrystal with curved grain boundaries have different values from those in the same polycrystal with flat grain boundary network.

4.2 Model Description

Two different 3D tetrahedral mesh elements are created from the same hypothetical digital polycrystal with 50 grains and the same list of crystallographic orientations for individual grains. One is the meshed microstructure with flat grain boundaries, and the other with curved grain boundaries (figures 13 and 14). For an FEM simulation, the length of each side of the meshed microstructure is

set to be 50mm. During the generation of the 3d mesh using HyperMesh, the mesh element size is set to have size of 1. The unit type is C3D4, which commands to generate tetrahedral elements to fill each volume defined by the input surface mesh. The total number of mesh elements are 497,884 and 491,856 for the flat boundary case and the curved boundary case, repectively.
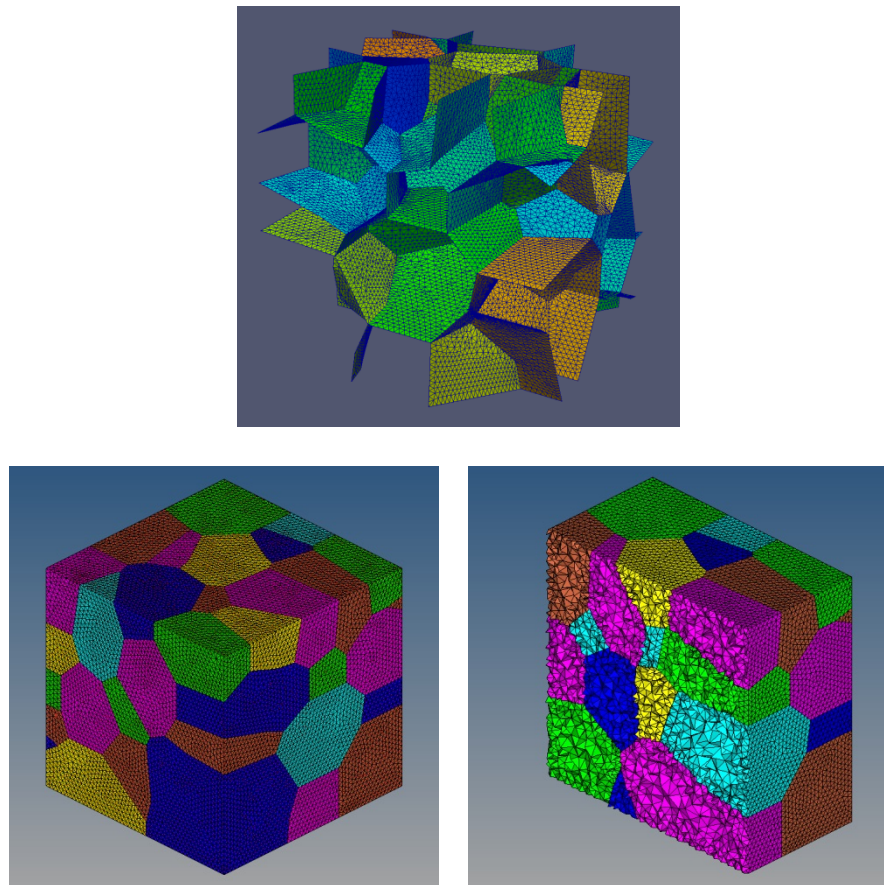
Figure 13. The tetrahedral mesh elements with flat grain boundaries on the hypothetical 3D digital microstructure
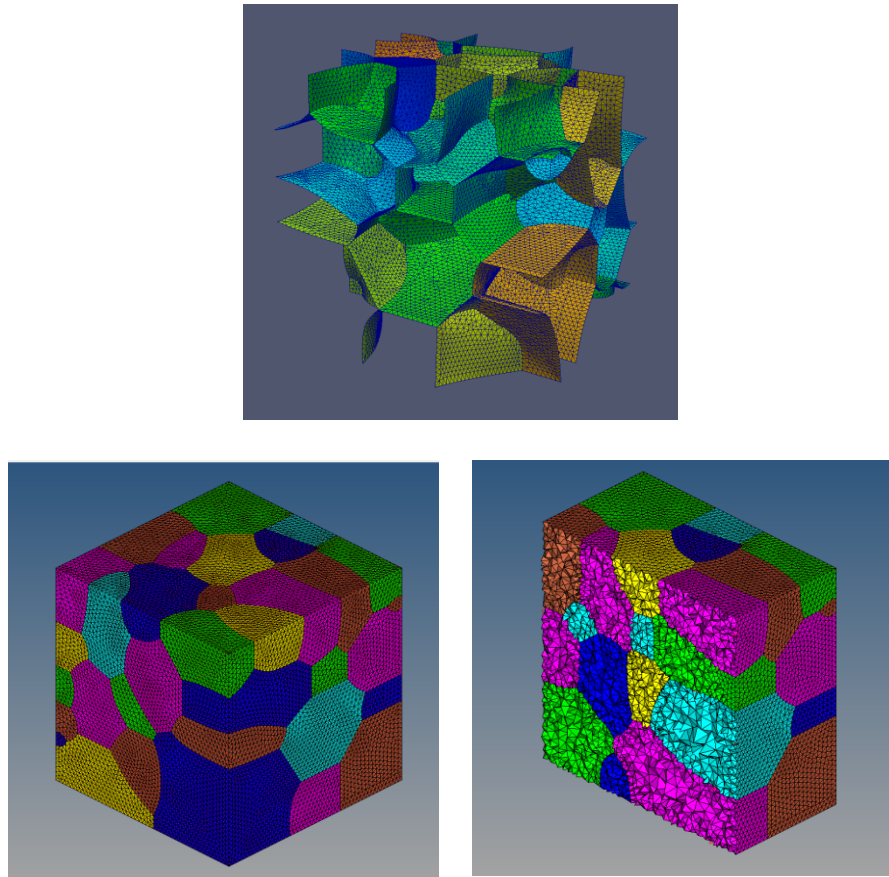
Figure 14. The tetrahedral mesh elements with curved grain boundaries on the hypothetical 3D digital microstructure

4.3 Parameter determination for an FEM simulation

To predict the internal mechanical field distribution of a polycrystalline material in cyclic thermal loading condition using a FEM simulation, a set of material properties of pure copper are used on a mesoscopic polycrystalline scale. The anisotropic nature of the properties of copper and the texture effect of the polycrystal is realized by using relevant tensors as inputs for the FEM simulation such that they are passively rotated and assigned to respective grains according to their crystallographic orientations. Here, we examine the elastic response of the polycrystal to a cyclic loading in one direction.

Specifically, a list of random orientations are assigned to grains, and the material model considers linear anisotropic elastic behavior. For a cubic copper, the elasticity stiffness coefficients

are known as follow:

$$C_{11} = 168GPa, \ C_{22} = 121GPa, \ C_{44} = 75GPa$$

The thermal expansion coefficient (α) of copper are given by: $16 \cdot 10^{-6} /^{\circ} C$

      For deriving the constitutive equations, we expand the model using Hooke's law to introduce the thermal expansion coefficient of part of the elastic strain to the total strain of the polycrystal.

$$\nabla \sigma_{ij} = \nabla [C_{ijkl} \varepsilon_{kl}^{elastic}] = 0 \tag{24}$$

$$C'_{ijkl} = A_{im} A_{jn} A_{ko} A_{ip} C_{mnop} \tag{25}$$

$$\varepsilon_{kl}^{elastic} = \varepsilon_{kl}^{total} - \varepsilon_{kl}^{thermal} = \varepsilon_{kl}^{total} - \alpha \Delta T \tag{26}$$

Equation (24) means states a simple Hooke's law. We understand that if there is no deformation, than no energy should be stored in the material. This would amount to the deformation gradient being equal to the identity tensor, or the finite strain tensor being zero.

      Stiffness coefficients and Thermal expansion coefficients are rotated by Bunge Euler angle sets (see appendix A). Because of the complexity in modifying the polycrystal model inside ABAQUS (in fact, one does that usually using UMAT, user material subroutine), all rotated material parameters are calculated using the in-house C code to make an input .inp file to ABAQUS. The script includes mesh data and the material properties (see appendix B).

      Boundary conditions are set automatically using the graphical user interface options provided in ABAQUS. The boundary conditions are such that the bottom face of the polycrystal (z = 0 mm) is fixed and the cyclic displacement of +0.03 mm and – 0.03 mm is homogeneously applied on top face (z = 50 mm). Therefore, when displacement is negative, a uniaxial compression is applied, and when positive, a uniaxial tension is applied as shown in figure 16. At the same time, the polycrystal is set to have a cyclic heating.

Displacement : 0.03mm
(copper's elastic region)

$\triangle T = 1000$℃
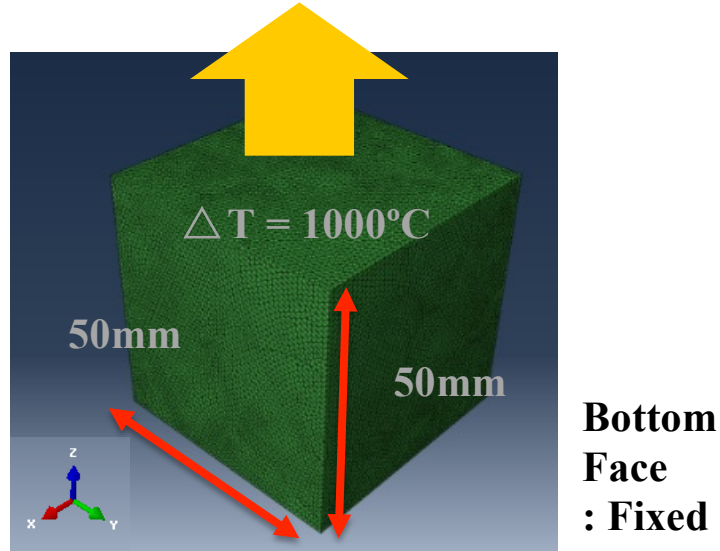
50mm

50mm

Bottom Face : Fixed

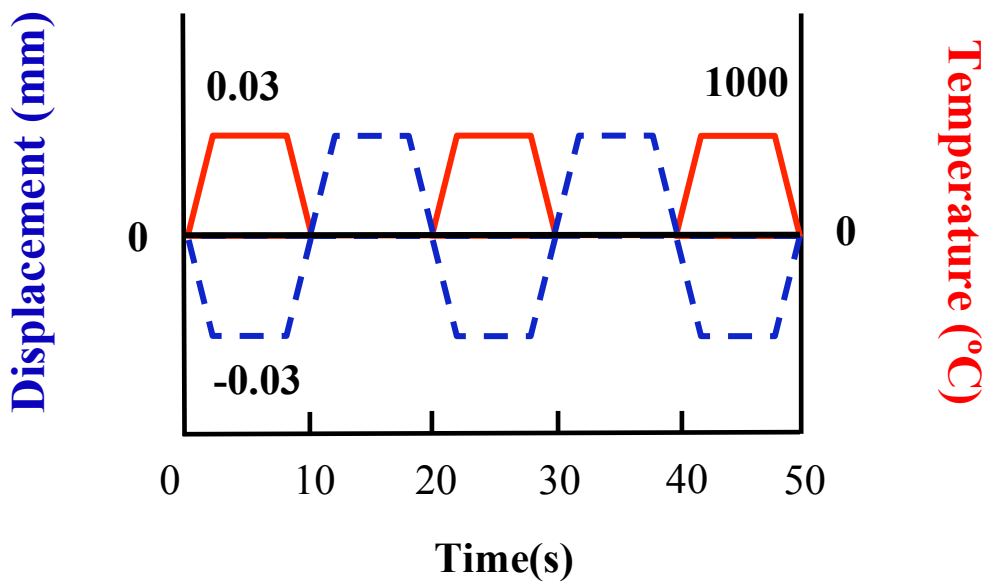Figure 15. Boundary conditions of the copper polycrystal in the FEM model

Figure 16. Displacement and temperature variation for the cyclic thermal loading simulation used in the FEM simulation

27

4.5 Results & Discussion

This section contains the results of the proposed FEM simulation on the Cu polycrystalline model using the cross-section analysis of the three dimensional microstructure under the cyclic thermal loading. Here, the corresponding cross-sections at the same position and simulation time inside both microstructures, with flat grain boundaries and curved grain boundaries are extracted and the values are compared to see if there is any difference in mechanical field aroused by the existence of the curvature of the grain boundary network.

Figure 17 shows the distributions of von Mises stress on the corresponding XY planes of two polycrystals, where Z = 36 mm at simulation time = 4 second. In general, the sections show the similar von Mises stress distribution with each other. The von Mises stress value of the microstructure with flat grain boundaries is 2,287 Mpa in the dotted circled area, while that of the microstructure with curved grain boundaries is 2,443 Mpa. The difference is 156 Mpa, showing approximately 7 % difference. Note that the gray color is bigger than the stress values with red color by an order, and the location and distribution of those gray areas are quite different with each other. Figures 18~20 show the distributions of selected normal stress and shear stress components. In the dotted area (figure 18), the stress values of microstructure with curved grain boundaries are more concentrated in spze. In figure 19, the local stress distribution is different in the marked area. Also, the microstructure with flat grain boundaries has higher stress value in the same area (figure 20).

Figures 21~23 indicate the corresponding strain distributions. As shown in figure 21, the local strain distributions, especially near the junctions, look different between those two microstructures. The high strain is located in the other spot in figure 22. In figures 24 ~ 26 are shown the strain energy density values. It is found that more energy is concentrated in the regions where both stress and strain are high. At Z axis = 36mm, the microstructure with flat grain boundaries has a higher strain energy density than the microstructure with curved grain boundaries (figure 26).

Figure 17. von Mises stress distribution on the XY plane with Z = 36 mm at simulation time = 4 second of 3D microstructure with (a) flat grain boundaries, and (b) curved grain boundaries

Figure 18. Stress 22 distribution on the XY plane with Z = 36 mm at simulation time = 4 second of 3D microstructure with (a) flat grain boundaries, and (b) curved grain boundaries
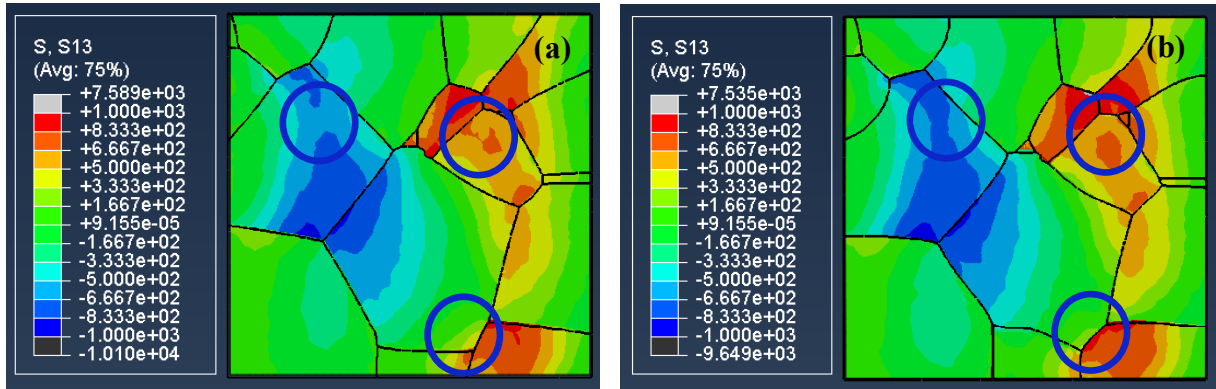
Figure 19. Stress 12 distribution on the XY plane with Z = 12 mm at simulation time = 4 second of
3D microstructure with (a) flat grain boundaries, and (b) curved grain boundaries
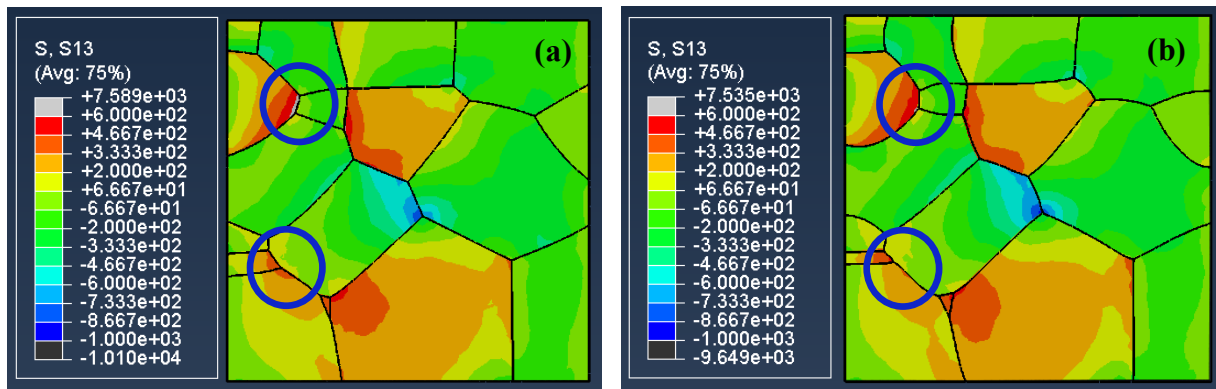
Figure 20. Stress 13 distribution on the XY plane with Z = 24 mm at simulation time = 4 second of
3D microstructure with (a) flat grain boundaries, and (b) curved grain boundaries
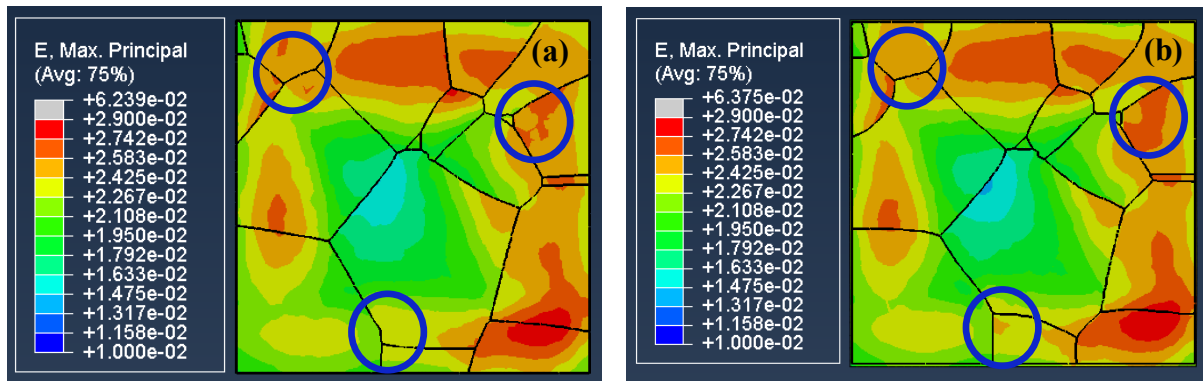
Figure 21. Strain distribution on the XY plane with Z = 12 mm at simulation time = 4 second of 3D microstructure with (a) flat grain boundaries, and (b) curved grain boundaries
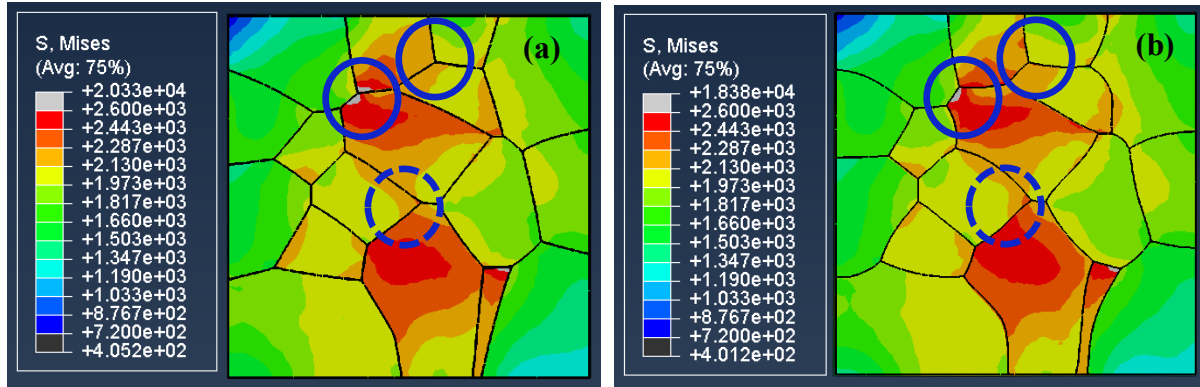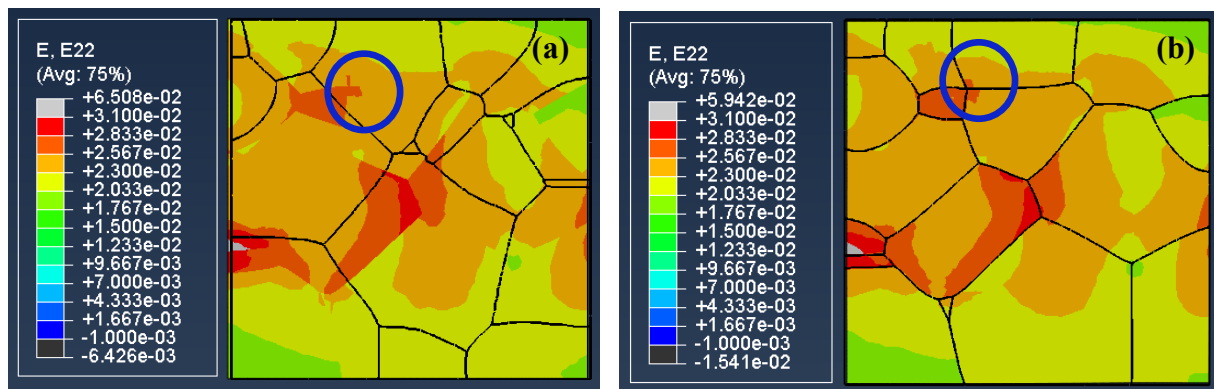

Figure 22. Strain 22 distribution on the XY plane with Z = 24 mm at simulation time = 4 second of 3D microstructure with (a) flat grain boundaries, and (b) curved grain boundaries
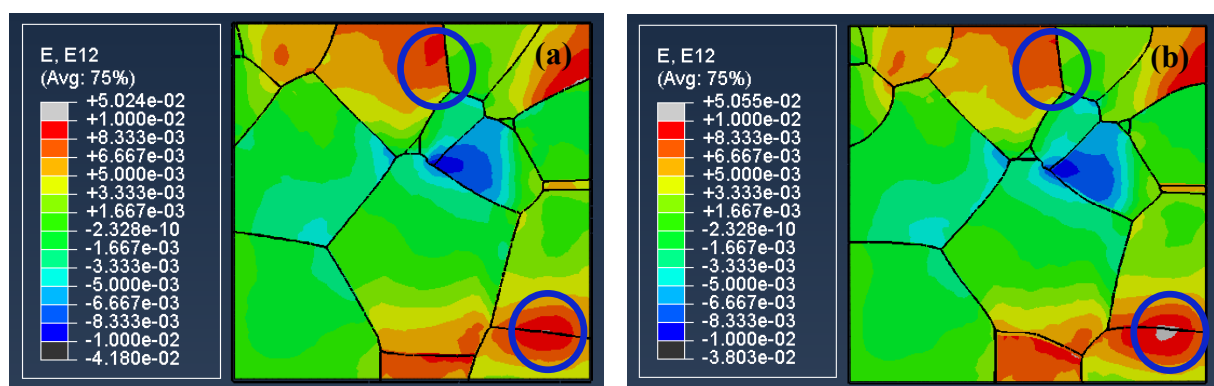
Figure 23. Strain 12 distribution o on the XY plane with Z = 12 mm at simulation time = 4 second of 3D microstructure with (a) flat grain boundaries, and (b) curved grain boundaries
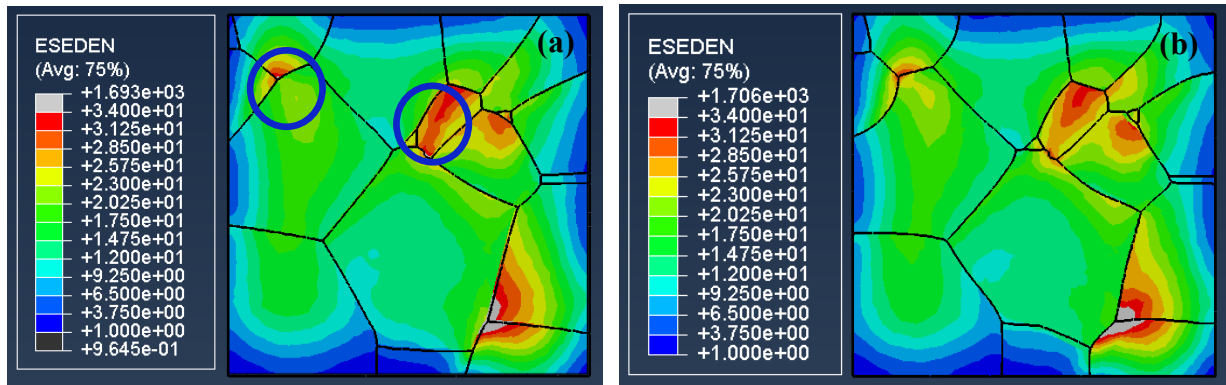
Figure 24. Elastic strain energy density distribution on the XY plane with Z = 12 mm at simulation time = 4 second of 3D microstructure with (a) flat grain boundaries, and (b) curved grain boundaries
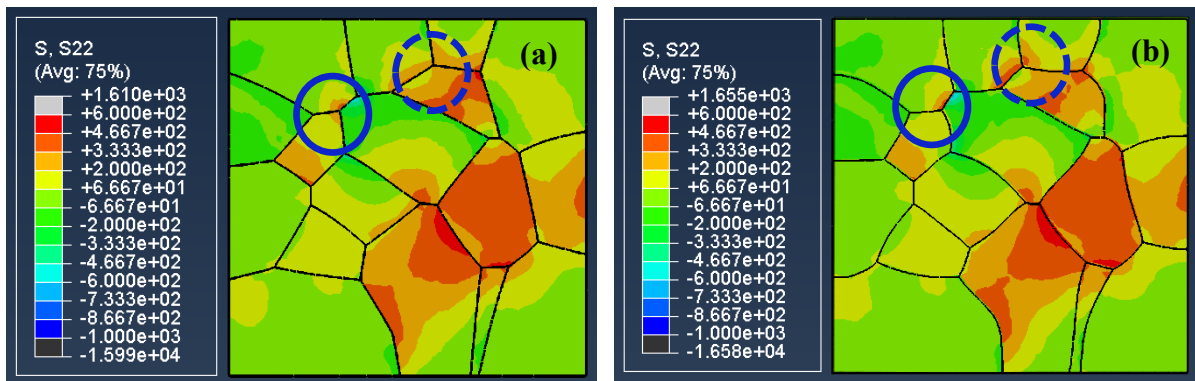

Figure 25. Elastic strain energy density distribution on the XY plane with Z = 24 mm at simulation time = 4 second of 3D microstructure with (a) flat grain boundaries, and (b) curved grain boundaries
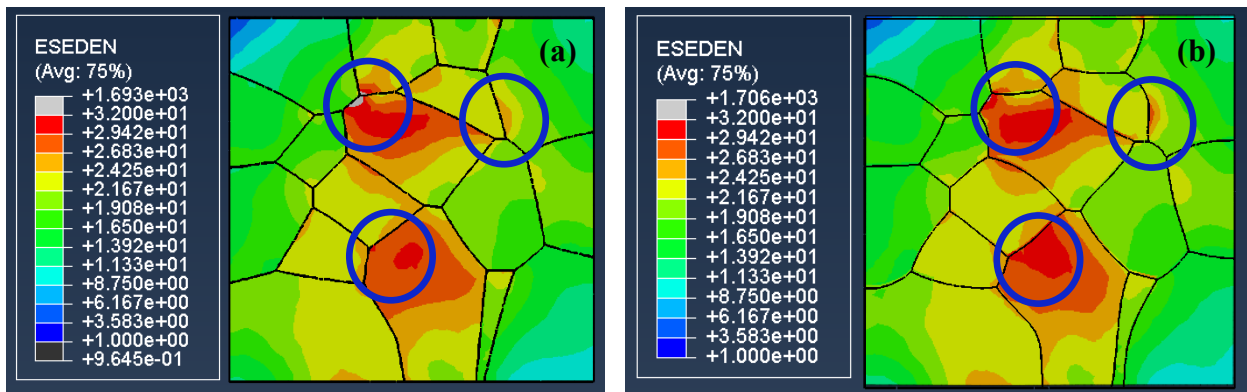
Figure 26. Elastic strain energy density distribution on the XY plane with Z = 36 mm at simulation time = 4 second of 3D microstructure with (a) flat grain boundaries, and (b) curved grain boundaries
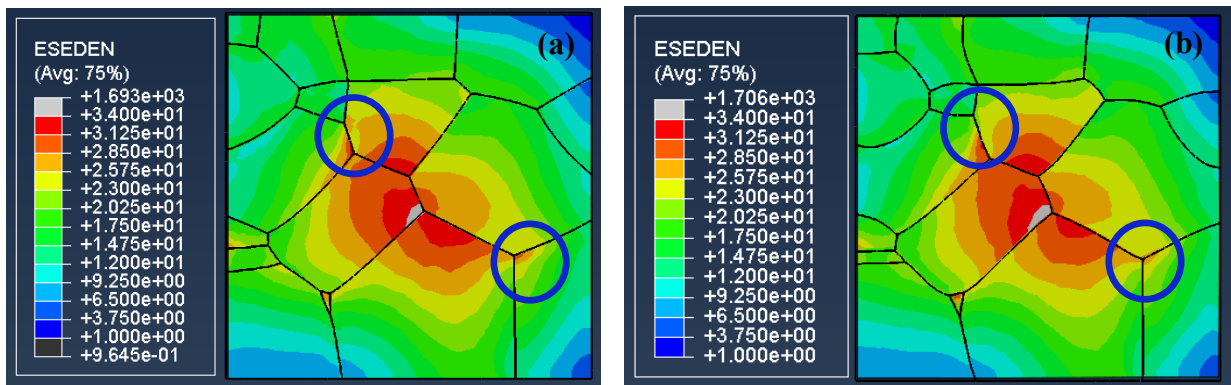
5. Conclusions

In this research, a new scheme for generating an FEM-suitable 3D polycrystalline mesh elements is proposed. Conducting the proposed scheme on the digital, voxellated polycrystalline image, we successfully improved the quality of the triangles on a surface grain boundary network mesh by using re-meshing techniques provided in a commercial program. The Jacobian value , the triangle minimum angle, and the aspect ratio of the original surface mesh much improved after applying the re-meshing technique. Using the enhanced surface mesh, we successfully created a polycrystalline microstructure filled with conformal 3d tetrahedral elements, collectively appropriate for an Finite Element Method simulation. Again, a couple of volumetric mesh generation techniques like standard and aggressive, provided by HyperMesh, were used to find the best mesh information for the polycrystal.

Using the created mesh data, we compared the difference in the mechanical fields distribution in the polycrystalline microstructure under cyclic thermal loading as we changed the curvature of the grain boundary network. We found that the locations and shapes of the hot spots of the stress and strain changed as the grain boundary curvature changed. But, we could not see the significant difference. This seems to be due to the nature of the elastic simulation, small number of grain sampling, and free surface effect not by applying the periodic boundary conditions. In the future, by simulating the accumulation of damages from non-severe plasticity or the high temperature creep behaviour, we might find the different evolution of mechanical fields due to the existence of the grain boundary curvature inside the polycrystal..

Appendix A. Euler Angle Determination

Euler angles are necessary for input into for the proposed FEM simulation using ABAQUS. Therefore, a C code for Euler angle determination has created and is shown in figure A.1~3. Three angles are required for rotation of the vector. Multiple grains has random orientations in figure A.4.

Code 1

```c
void read_euler_angles(struct orient *aB, int nAng, char ifn[255]){

    int i;
    int dummyi;
    double te1, te2, te3; // Temporary euler angle
    double dummyf;

    FILE *f;

    char trash[255];

    if((f= fopen(ifn, "r"))==NULL){
        printf("\tcannot find the input orientation list file...\n");
        exit(0);
    }

    // get rid of header lines..
    fgets(trash, 255, f);
    for(i=0; i<=nAng; i++){
        fscanf(f, "%d %d %d %d %lf %lf %lf %lf",
                &dummyi, &dummyi, &dummyi, &dummyi, &te1, &te2, &te3, &dummyf);

    // degree converted into radian
        te0 = te0*PI/180;
        te1 = te1*PI/180;
        te2 = te2*PI/180;

        aB[i].euler[0] = te1;
        aB[i].euler[1] = te2;
        aB[i].euler[2] = te3;

    }
    fclose(f);
}
```

Figure A.1 C function to read Euler angles

Code 2

```c
void read_old_4th_rank_tensor(double oldS[4][4][4][4]){

    int i, j, k, l;
    FILE *f;
    char trash[255];

    if((f= fopen(fourth_rank_tensor_filename, "r"))==NULL){
        printf("\tcannot find the input old stiffness tensor file...\n");
        exit(0);
    }

    // initializing the 4th rank tensor[4][4][4][4], before reading 4th rank tensor file
    for(i=0; i<4; i++){
        for(j=0; j<4; j++){
            for(k=0; k<4; k++){
                for(l=0; l<4; l++){
                    oldS[i][j][k][l] = 0;
                }
            }
        }
    }

    // get rid of header lines..
    fgets(trash, 255, f);
    for(i=1; i<4; i++){
        for(j=1; j<4; j++){
            for(k=1; k<4; k++){
                for(l=1; l<4; l++){
                    fscanf(f, "%lf", &oldS[i][j][k][l]);
                }
            }
        }
    }

    fclose(f);
}
```

Figure A.2 C function to read old fourth rank tensor

```
void rotate_4th_rank_tensor(struct orient *aB, double oldS[4][4][4][4], double newS[4][4][4][4])

  int z;
  int i, j, k, l;
  int m, n, o, p;
  double matrix[4][4]; // Rotation matrix

  // 1. constructing rotation matrix using Bunge Euler angle set
  matrix[1][1] = cos(aB[z].euler[0])*cos(aB[z].euler[2])-sin(aB[z].euler[0])*sin(aB[z].euler[2])*
              cos(aB[z].euler[1]);
  matrix[1][2] = sin(aB[z].euler[0])*cos(aB[z].euler[2])+cos(aB[z].euler[0])*sin(aB[z].euler[2])*
              cos(aB[z].euler[1]);
  matrix[1][3] = sin(aB[z].euler[2])*sin(aB[z].euler[1]);
  matrix[2][1] = -cos(aB[z].euler[0])*sin(aB[z].euler[2])-sin(aB[z].euler[0])*cos(aB[z].euler[2])*
              cos(aB[z].euler[1]);
  matrix[2][2] = -sin(aB[z].euler[0])*sin(aB[z].euler[2])+cos(aB[z].euler[0])*cos(aB[z].euler[2])*
              cos(aB[z].euler[1]);
  matrix[2][3] = cos(aB[z].euler[2])*sin(aB[z].euler[1]);
  matrix[3][1] = sin(aB[z].euler[0])*sin(aB[z].euler[1]);
  matrix[3][2] = -cos(aB[z].euler[0])*sin(aB[z].euler[1]);
  matrix[3][3] = cos(aB[z].euler[1]);

  // 2. transforming of 4th rank tensor
     for(i=1; i<4; i++)
       for(j=1; j<4; j++)
         for(k=1; k<4; k++)
           for(l=1; l<4; l++)
             for(m=1; m<4; m++)
               for(n=1; n<4; n++)
                 for(o=1; o<4; o++)
                   for(p=1; p<4; p++)
         newS[i][j][k][l]+=matrix[m][i]*matrix[n][j]*matrix[o][k]*matrix[p][l]*oldS[m][n][o][p];

  // 3. writing the results of transformation for ABAQUS
  fprintf(f,"%10.3e, %10.3e, %10.3e, %10.3e, %10.3e, %10.3e, %10.3e, %10.3e\n %10.3e,
  %10.3e, %10.3e, %10.3e, %10.3e, %10.3e, %10.3e, %10.3e\n %10.3e, %10.3e, %10.3e,
  %10.3e, %10.3e\n",
  newS[1][1][1][1], newS[1][1][2][2], newS[2][2][2][2], newS[1][1][3][3], newS[2][2][3][3],
  newS[3][3][3][3], newS[1][1][1][2], newS[2][2][1][2], newS[3][3][1][2], newS[1][2][1][2],
  newS[1][1][1][3], newS[2][2][1][3], newS[3][3][1][3], newS[1][2][1][3], newS[1][3][1][3],
  newS[1][1][2][3], newS[2][2][2][3], newS[3][3][2][3], newS[1][2][2][3], newS[1][3][2][3],
  newS[2][3][2][3])
```

Figure A.3 C function to rotate fourth rank tensor

	ϕ_1	Φ	ϕ_2		ϕ_1	Φ	ϕ_2
Grain 1	198.86	71.87	57.97	**Grain 26**	311.47	32.58	150.31
Grain 2	152.34	98.38	204.25	**Grain 27**	181.15	64.16	80.99
Grain 3	290.68	27.49	31.19	**Grain 28**	13.10	100.44	110.55
Grain 4	106.3	79.22	160.42	**Grain 29**	317.42	162.06	263.38
Grain 5	137.53	105.76	16.27	**Grain 30**	62.94	66.50	271.67
Grain 6	101.9	154.58	110.05	**Grain 31**	211.45	118.48	247.06
Grain 7	71.66	120.95	115.58	**Grain 32**	203.36	129.23	288.39
Grain 8	126.61	20.28	350.44	**Grain 33**	222.18	156.97	343.32
Grain 9	185.5	58.25	202.93	**Grain 34**	50.02	57.50	325.90
Grain 10	60.52	52.39	266.37	**Grain 35**	354.73	87.58	327.62
Grain 11	282.74	59.33	42.27	**Grain 36**	81.26	155.10	44.38
Grain 12	228.14	70.81	334.46	**Grain 37**	241.11	96.21	23.66
Grain 13	255.3	155.14	331.25	**Grain 38**	130.79	49.01	1.47
Grain 14	51.86	106.15	246.18	**Grain 39**	327.86	78.85	26.94
Grain 15	37.41	29.68	1.49	**Grain 40**	165.07	58.83	47.98
Grain 16	248.39	110.76	175.89	**Grain 41**	105.32	113.35	177.83
Grain 17	86.05	136.88	94.36	**Grain 42**	79.61	80.02	19.79
Grain 18	164.11	98.01	198.53	**Grain 43**	206.81	84.77	55.44
Grain 19	169.28	53.51	193.73	**Grain 44**	271.80	50.40	287.30
Grain 20	189.83	58.84	179.31	**Grain 45**	269.20	152.31	234.80
Grain 21	308.95	58.52	8.43	**Grain 46**	310.20	125.67	145.91
Grain 22	339.33	26.69	327.5	**Grain 47**	142.68	115.46	341.81
Grain 23	123.01	96.01	129.63	**Grain 48**	98.31	99.66	203.78
Grain 24	127.89	23	201.54	**Grain 49**	166.36	115.40	276.32
Grain 25	24	150.68	353.06	**Grain 50**	167.45	16.95	46.38

Figure A.4 Euler angle specification for multiple grains

Appendix B. ABAQUS input file

The large box in figure B.1 contains all of the material properties. Figure B.2 shows a step specification portion of input file with the important aspects highlighted. The box directly under "*STATIC" contains time value which dictate how the step is to be performed. The first value is the time increment for step. The next value is total time that the step should consume. The box underneath "*TEMPERATURE" contains the temperature at the end of the step. The dashed box contains temperature for the history.

```
**   MATERIALS
*Material, name=MATERIAL-0
*Elastic, type=ANISOTROPIC
180100.,117700.,176900.,112300.,115400.,182300.,   740.5,   5423.
  11060., 72070., 39550., 29210., 39940., 20840., 66660., 30620.
  43840., 42050., 13710.,        0., 69810.
*Expansion, type=ANISO
 1.6e-05,   1.6e-05,   1.6e-05,          0., 5.371e-06, 5.428e-06
*Material, name=MATERIAL-1
*Elastic, type=ANISOTROPIC
183700.,112400.,178200.,113800.,119300.,176800., 44380., 51920.
  35710., 66840., 36230., 27000., 41460., 14170., 68240., 10380.
   2793.,   694.5, 15540., 30120., 73750.
*Expansion, type=ANISO
 1.6e-05,   1.6e-05,   1.6e-05, 6.444e-06, 5.068e-06,          0.
*Material, name=MATERIAL-2
*Elastic, type=ANISOTROPIC
185100.,110200.,182600.,114700.,117200.,178000., 45630., 48600.
  47070., 64600.,   2029.,   2034.,   7356., 26230., 69130., 14470.
  12290., 15010.,   8824., 34020., 73210.
*Expansion, type=ANISO
 1.6e-05,   1.6e-05,   1.6e-05, 7.472e-06,          0., 2.441e-06

                        ~

*Material, name=MATERIAL-49
*Elastic, type=ANISOTROPIC
180500.,109900.,182300.,119700.,117800.,172500.,   4988.,   4787.
   2771., 64270., 22150.,   7529., 21860., 16220., 74070., 29460.
  33710., 41840., 15700.,   2771., 72210.
*Expansion, type=ANISO
 1.6e-05,   1.6e-05,   1.6e-05, 2.884e-07, 2.782e-06, 4.355e-06
```

Figure B.1 Material input section of a input file

```
**
** STEP: Step-1
**
*Step, name=Step-1
*Static, direct
1., 50.,
**
** BOUNDARY CONDITIONS
**
** Name: Disp-BC-2 Type: Displacement/Rotation
*Boundary, amplitude=AMP-2
SET-2, 3, 3, 0.03
**
** PREDEFINED FIELDS
**
** Name: Field-2    Type: Temperature
*Temperature, amplitude=AMP-1
SET-4, 1000.
**
** OUTPUT REQUESTS
**
*Restart, write, frequency=0
**
** FIELD OUTPUT: F-Output-1
**
*Output, field, variable=PRESELECT
**
** HISTORY OUTPUT: H-Output-1
**
*Output, history, variable=PRESELECT
*End Step
```

Figure B.2 Step specification section of input file

References

[1] Smith C 1948. Trans. Grains, phases and interfaces : An interpretation of microstructures. Am. Inst. Min. Metall. Eng. **175** 15

[2] Williams W and Smith C 1952. Study of grain shape in an aluminum alloy and other applications of stereoscopic microradiography. Trans. Am. Inst. Min. Metall. Eng. **194** 755

[3] Quey R, Dawson P R and Barbe F, 2011. Large-scale 3D random polycrystals for the finite element method: Generation, meshing and remeshing. Comput. Methods Appl. Mech. Eng. **200** 1729

[4] Bhandari Y, Sarkar S, Groeber M, Uchic M, Dimiduk D M and Ghosh S, 2007. 3D polycrystalline microstructure reconstruction from FIB generated serial sections for FE analysis. Comput. Mater. Sci. **41** 222

[5] Ghosh S, Bhandari Y and Groeber M, 2008. CAD-based reconstruction of 3D polycrystalline alloy microstructures from FIB generated serial sections. Comput. –Aided Des. **40** 293

[6] Miranda A C O, Martha L F, Wawrzynek P A and Ingraffea A R, 2009. Surface mesh regeneration considering curvatures. Eng. Comput. **25** 207

[7] Kuprat A, Khamayseh A, Geroge D and Larkey L, 2001. Volume conserving smoothing for piecewise linear curves, surfaces and triple lines. J. Comput. Phys. **172** 99

[8] Moore R H, Rohrer G S and Saigal S, 2009. Reconstruction and simplification of high-quality multiple-region models from planar sections. Eng. Comput. **25** 221

[9] J. Montalvo-Urquizo, P. Bobrov, A. Schmidt, W. Wosniok, 2012. Elastic response of texturized microscale materials using FEM simulations and stochastic material properties. Mech. Mater. **47** 1-10

[10] C.N. N'Guyen, F. Barbe, N. Osipov, G. Cailletaud, B. Marini, C. Petry, 2012. Micromechanical local approach to brittle failure in bainite high resolution polycrystals. Comput. Mater. Sci. **64** 62-65

[11] Masayuki Kamaya, Yoshihiro Kawamura, Takayuki Kitamura, 2007. Three dimensional local stress analysis on grain boundaries in polycrystalline material. Solids and structrues. **44** 3267-3277

[12] Fabrice Barbe, Romain Quey, Andrei Musienko, Georges Cailletaud, 2009. Three-dimensional characterization of strain localization bands in high-resolution elastoplastic polycrystals. Mech. Research Comm. **36** 762-768

[13] Su Leen Wong, Mark Obstalecki, Matthew P. Miller, Paul R. Dawson, 2015. Stress and deformation heterogeneity in individual grains within polycrstals subjected to fully reversed cyclic loading. Mech. Phys.

[14] Feihu Gao, Yongjin Chen, Ran Guo, K. Wang, Y. Huang, 2014. FEM analysis on a tensile loaded copper plate in meso and macro scale. Mech. Mater. 444-445

[15] Taylor and Francis group, Introduction to texture analysis

[16] J. F. NYE, F.R.S. Physical properties of crystals

[17] S-B Lee, G S Rohere, A D Rollet, 2014. Three-dimensional digital approximations grain boundary networks in polycrystals. Modelling Simul. Mater. Sci. Eng. **22** 025017

[18] Maximilien Livert, Colette Rey, Ludovic Vincent, Bernard Marini, 2011. Temperature dependent polycrystal model application to bainitic steel behavior under tri-axial loading in the ductile-brittle transition. Solids and Structrues. **48** 2196-2208

[19] Wan Jian-song, YUE Zhu-feng, 2004. Stress distribution near grain boundary in anisotropic bicrystals and tricrystals. Math. Mech. **25** 1

Acknowledgements